# Hard X-ray imaging microscopy with self-imaging phenomenon

| | |
|---|---|
| 著者 | Wataru Yashiro |
| journal or publication title | Microscopy |
| volume | 67 |
| number | 6 |
| page range | 303-316 |
| year | 2018-10-11 |
| URL | http://hdl.handle.net/10097/00126459 |

doi: 10.1093/jmicro/dfy040

# Hard X-ray imaging microscopy with self-imaging phenomenon

Wataru Yashiro

Institute of Multidisciplinary Research for Advanced Materials (IMRAM), Tohoku University

Katahira 2-1-1, Aoba-ku, Sendai 980-8577, Japan

Tel & Fax: +81-22-217-5184

E-mail address: wataru.yashiro.a2@tohoku.ac.jp

Keywords: X-ray imaging, X-ray microscopy, grating, Talbot effect, interferometry

Total number of pages: 37

Total number of figures: 8

# Abstract

The self-imaging phenomenon referred to as the Talbot effect in the field of optics was discovered by H. F. Talbot in the 1830s, and is now widely used for imaging using not only visible light but also X-rays, electrons, neutrons, and matter waves. In this review, the author introduces the current progress being made in hard-X-ray imaging microscopy based on the self-imaging phenomenon. Hard-X-ray imaging microscopy is a promising technique for non-destructively visualizing internal structures in specimens with a spatial resolution up to a few tens of nanometers. The use of the self-imaging phenomenon makes it possible to realize highly sensitive phase-contrast X-ray imaging microscopes. These approaches have several advantages over conventional X-ray imaging microscopes, including the widely used Zernike X-ray phase-contrast microscopes, and can provide a powerful way of quantitative visualization with a high spatial resolution and a high sensitivity even for thick specimens.

## 1. Introduction

Non-destructive and quantitative high-spatial-resolution visualization of internal structures of materials consisting of light elements will bring about significant progress in biological and materials sciences. Hard-X-ray imaging microscopy is a technique for non-destructively visualizing internal structures of specimens with a spatial resolution up to a few tens of nanometers [1]. It has an advantage over other X-ray microscopies such as X-ray scanning and diffraction microscopies in that it does not require time-consuming measurements. However, similar to the other X-ray microscopies, it is less sensitive to materials consisting of lighter elements because hard X-rays weakly interact with them. One way to improve the sensitivity of hard-X-ray imaging microscopy is by using the phase-shift of X-rays passing through a specimen [2-4]. In principle, this so-called X-ray phase-contrast imaging microscopy provides three orders of magnitude higher sensitivity than conventional ones based on absorption contrast. Several X-ray phase-contrast imaging microscopes have been reported since the mid-1990s, but they require a high-brilliance synchrotron X-ray source or specially designed optics. Zernike phase-contrast microscopy for visible light [5,6] is attainable even for hard X-rays [7-10] and it works with a compact low-brilliant laboratory X-ray source, but it is quantitative only for a week-phase object.

In the last decade, X-ray phase-contrast imaging techniques using the self-images (referred to as “Fourier images” [11] in the field of electron microscspy) of a grating generated by the

Talbot effect [12-16], which is called X-ray grating interferometry [17-52], have attracted much attention. Because X-ray grating interferometry enables highly sensitive X-ray imaging with a continuous-spectrum low-brilliant laboratory X-ray source, it is suitable for medical diagnostics. Besides, it works with spherical-wave X-rays, which cannot be used other X-ray phase-contrast imaging techniques such as crystal interferometry and diffraction enhanced imaging (DEI). This fact enables the use of an X-ray lens, and X-ray phase-contrast imaging microscopes can be constructed on the basis of X-ray grating interferometry [27,29,30,32,34,40,50].

In this review, X-ray phase-contrast imaging microscopy is reviewed. The next section is devoted to the theoretical description of the self-imaging phenomenon. In Section 3, X-ray phase-contrast imaging using the X-ray grating interferometry is reviewed. In Section 4, several phase-contrast X-ray imaging microscopes using the self-imaging phenomenon are introduced. Finally, in Section 5, the future prospects of the X-ray imaging microscopes are discussed and conclusions are made.

## 2. Self-imaging phenomenon

The self-imaging phenomenon called the Talbot effect was discovered by H. F. Talbot [12]. A typical setup where the phenomenon can be observed is shown in Fig. 1, where spatially coherent quasi-monochromatic light emanated from a point source illuminates a one-dimensional periodic pattern (diffraction grating) located on the $(x_1, y_1)$-plane at a distance

$R_1$ from the source. When the pitch $d_1$ of the grating is much larger than the wavelength λ of the light, the images of the grating, called self-images or Talbot images, are formed at specific distances downstream of the grating.

This self-imaging phenomenon can be attributed to the Fresnel diffraction by the grating as follows. For simplicity, we consider the electric field of light close to the optical axis ($z$-axis). In addition, we assume that the electric field is polarized in the $y$-direction, but the following theoretical description is approximately correct even that polarized in the $x$-direction because only the Fresnel diffraction close to the optical axis (in the paraxial approximation) contributes to the self-imaging phenomenon. The electric field $E_2$ on the $(x_2, y_2)$-plane at a distance $z_{12}$ downstream from the grating can be written in the paraxial approximation by

$$E_2(x_2, y_2) \approx \frac{-iE_{10}}{\lambda} \frac{\exp\left[2\pi i \frac{z_{12}}{\lambda}\right]}{z_{12}} \iint T(x_1 + x', y_1 + y') \exp\left[\frac{i\pi({x'}^2 + {y'}^2)}{\lambda z_{\mathrm{eff},12}}\right] dx' dy'. \quad (1)$$

Here, $E_{10} \equiv \frac{E_0 \exp\left[2\pi i \frac{R_1}{\lambda}\right] \exp\left[\frac{\pi i ({x_1}^2 + {y_1}^2)}{\lambda R_1}\right]}{R_1}$ corresponds to the electric field just in front of the grating, $T(x_1, y_1)$ is the complex transmission function of the grating, $z_{\mathrm{eff},12}$ is the effective distance defined by $z_{\mathrm{eff},12} \equiv \left(\frac{1}{R_1} + \frac{1}{z_{12}}\right)^{-1}$, and $(x_2, y_2) \equiv \frac{R_2}{R_1}(x_1, y_1)$, where $R_2 \equiv R_1 + z_{12}$. If we assume that the size of the grating is regarded to be infinite, $T(x_1, y_1)$ can be expanded by a Fourier series $\sum_n a_n \exp\left[2\pi i \frac{n x_1}{d_1}\right]$, where $a_n$ is the $n$th Fourier component of the transmission function. Using $a_n$, Eq. (1) can be rewritten by

$$E_2(x_2, y_2) \approx E_{20} \sum_n b_n \exp\left[2\pi i \frac{n x_2}{d_2}\right], \quad (2)$$

where $E_{20} \equiv \frac{E_0 \exp\left[2\pi i \frac{R_2}{\lambda}\right] \exp\left[\frac{\pi i ({x_2}^2 + {y_2}^2)}{\lambda R_2}\right]}{R_2}$ corresponding to the electric field on the $(x_2, y_2)$-

plane when no grating would be placed, $d_2 \equiv \frac{R_2}{R_1} d_1$, and $b_n$ is defined by

$$b_n \equiv a_n \exp\left[-i\pi \frac{n^2 \lambda z_{\mathrm{eff},12}}{{d_1}^2}\right]. \quad (3)$$

Equation (3) means that if $z_{\mathrm{eff},12}$ is an even-integer multiple of $\frac{{d_1}^2}{\lambda}$, the electric field just behind the grating is completely reproduced with a magnification of $\frac{R_2}{R_1}$. This reproduction of the electric field forms the self-image. Historically, the effective distance where the first self-image appears, i.e., $\frac{2{d_1}^2}{\lambda}$, which was first found for nearly plane-wave illumination by Rayleigh [53], is called the Talbot distance. Note that even at an odd-integer multiple of $\frac{{d_1}^2}{\lambda}$, the electric field just behind the grating is also reproduced but with a half-pitch shift.

It is convenient to define the Talbot order $p$ by

$$p \equiv \frac{\lambda z_{\mathrm{eff},12}}{{d_1}^2} \,. \quad (4)$$

By using $p$, Eq. (3) can be rewritten as

$$b_n(p) \equiv a_n \exp[-i\pi n^2 p] \,, \quad (5)$$

In the cases where an absorption grating is used, the intensity of light just behind the grating is reproduced with a magnification of $\frac{R_2}{R_1}$ when $p$ is a positive integer (the intensity is shifted by a half pitch when $p$ is an odd positive integer). In the cases where a phase grating is used, an intensity distribution that is the same as the shape of the grating, which is also called a self-image, often appears at a fractional Talbot order. This phenomenon is referred to as the fractional Talbot effect. For example, when a rectangular $\pi/2$-phase grating with a duty cycle of 0.5 is used, its self-images appear at odd-integer multiples of $\frac{1}{2}$ [54], whereas when a rectangular π-phase grating with a duty cycle of 0.5 is used, its self-images with a compression ratio α of 2 (meaning that the pitch of a self-image is given by $\frac{d_2}{2}$) appear at odd-integer multiples of $\frac{1}{8}$ [55]. At a Talbot order other than such specific Talbot orders, various intensity distribution, which is generally referred to as the Fresnel image [56], appears.

Note that in the case of two dimensional grating, the Talbot distance is given by the minimum distance where $\lambda z_{\mathrm{eff},12}|N\boldsymbol{a}_1^* + M\boldsymbol{a}_2^*|$ is equal to an even integer for all $N$ and $M$ [56]. Here, $N$ and $M$ are integers and $\boldsymbol{a}_1^*$ and $\boldsymbol{a}_2^*$ are reciprocal lattice vectors defined by the primitive lattice vectors $\boldsymbol{a}_1$ and $\boldsymbol{a}_2$ of the two dimensional grating.

We can interpret Eq. (2) in geometrical wave optics [52]. In fact, we can rewrite Eq. (2) into

$$E_2(x_2, y_2) \approx E_{20} \sum_n T_n(x_1 - \Delta x_n) \exp\left[2\pi i \frac{\Delta l_n}{\lambda}\right], (6)$$

where

$$T_n(x_1) \equiv a_n \exp\left[2\pi i \frac{n x_1}{d_1}\right], (7)$$

$$\Delta x_n \equiv n \frac{\lambda}{d_2} z_{12}, (8)$$

$$= n p d_1, (9)$$

$$\Delta l_n \equiv \frac{{\Delta x_n}^2}{2 z_{\mathrm{eff},12}}. (10)$$

Equation (6) can be interpreted as follows: the $n$th order diffracted wave propagates along the path passing through the point $P_n$ shown in Fig. 2, and $\Delta l_n$ corresponds to the optical path difference between the $n$th and 0th orders, passing through the points $P_n$ and $P_0$, respectively.

The intensity $I_2(x_2, y_2)$ of the image at the distance of $z_{12}$ from the grating is given by

$$I_2(x_2, y_2) \approx I_{20} \sum_m T_{m+n}(x_1 - \Delta x_{m+n}) T_m^*(x_1 - \Delta x_m) \exp\left[2\pi i \frac{\Delta l_{m+n} - \Delta l_m}{\lambda}\right], \quad (11)$$

where $I_{20} \equiv |E_{20}|^2$. Equation (11) is convenient when we consider the effect of spatial and temporal coherences of light: the spatial- and temporal-coherence lengths on the grating that are required for $m$th and $(m+n)$th orders to interfere are given by $\Delta x_n$ and $\Delta l_n$, respectively. For a finite size of quasi-monochromatic light source, the effect of the spatial coherence can be described by the van Cittert-Zernike theorem [6,15] and can be represented by a complex coherence factor $\mu_n$ [6]; using $\mu_n$, $I_2(x_2, y_2)$ can be expressed in the following form [47]:

$$I_2(x_2, y_2) \approx I_{20} \sum_m \mu_n T_{m+n}(x_1 - \Delta x_{m+n}) T_m^*(x_1 - \Delta x_m) \exp\left[2\pi i \frac{\Delta l_{m+n} - \Delta l_m}{\lambda}\right]. \quad (12)$$

For the self-image to be observed, it is necessary for the $m$th and $(m+1)$th orders to interfere. Because the $m$th and $(m+1)$th order waves propagate along two different paths separated by $pd_1$ on the grating (see Fig. 2), a spatial coherence length that is comparable or larger than $pd_1$ is necessary on the grating. On the other hand, the self-image can be observed even for a broad spectrum because, from the Wiener-Khintchine's theorem [6], the temporal coherence length of the light used is roughly given by $\frac{\lambda^2}{\Delta\lambda}$, where $\Delta\lambda$ is the bandwidth of the light, and the temporal coherence that is necessary for the $m$th and $(m+1)$th orders to interfere is $\Delta l_1$, which is comparable to $\lambda$ when $d_1 \gg \lambda$.

## 3. X-ray grating interferometry

In the X-ray grating interferometry based on the Talbot effect, the phase shift caused by a sample is detected by the deformation of the self-image. When a sample is located at a distance of $R_\mathrm{s}$ from the X-ray source in Fig. 1, the electric field on the $(x_2, y_2)$-plane is expressed from Eqs. (2) and (6) by [47]

$$E_2(x_2, y_2) \approx E_{20} \sum_n b_n(p) T'_\mathrm{s}(x_\mathrm{s} - np_\mathrm{s}d_1, y_\mathrm{s}) \exp\left[2\pi i \frac{nx_2}{d_2}\right]. \quad (13)$$

Here, $(x_\mathrm{s}, y_\mathrm{s}) \equiv \frac{R_\mathrm{s}}{R_1}(x_1, y_1)$, $p_\mathrm{s}$ is the effective Talbot order given by

$$p_\mathrm{s} \equiv \begin{cases} p\frac{R_\mathrm{s}}{R_1} & (0 \leq R_\mathrm{s} \leq R_1) \\ p\frac{R_2 - R_\mathrm{s}}{R_2 - R_1} & (R_1 \leq R_\mathrm{s} \leq R_2) \end{cases}, \quad (14)$$

and $E_{20}T'_\mathrm{s}(x_\mathrm{s}, y_\mathrm{s})$ corresponds to the electric field on the $(x_2, y_2)$-plane that formed because of the free-space propagation of X-rays from the sample to the plane when no grating is located: $T'_\mathrm{s}(x_\mathrm{s}, y_\mathrm{s})$ is expressed using the complex transmission function $T_\mathrm{s}(x_\mathrm{s}, y_\mathrm{s})$ of the sample by

$$T'_\mathrm{s}(x_\mathrm{s}, y_\mathrm{s}) \approx \iint T_\mathrm{s}(x_\mathrm{s} + x'_\mathrm{s}, y_\mathrm{s} + y'_\mathrm{s}) \exp\left[\frac{i\pi({x'_\mathrm{s}}^2 + {y'_\mathrm{s}}^2)}{\lambda z_\mathrm{eff,s2}}\right] dx'dy', \quad (15)$$

where $z_\mathrm{eff,s2} \equiv \left(\frac{1}{R_\mathrm{s}} + \frac{1}{R_2 - R_\mathrm{s}}\right)^{-1}$. The complex transmission function $T_\mathrm{s}(x_\mathrm{s}, y_\mathrm{s})$ of the sample represents the effects of the absorption and the phase-shift of the sample:

$$T_\mathrm{s}(x_\mathrm{s}, y_\mathrm{s}) = \exp\left[-\frac{\mu_\mathrm{s}(x_\mathrm{s}, y_\mathrm{s})}{2}\right] \exp[-i\Phi(x_\mathrm{s}, y_\mathrm{s})] \quad , (16)$$

where $\mu_\mathrm{s}(x_\mathrm{s}, y_\mathrm{s})$ corresponds to the linear absorption coefficient and $\Phi(x_\mathrm{s}, y_\mathrm{s})$ is the phase shift caused by the sample. The intensity of the self-image is expressed from Eqs. (12) and (13) by

$$I_2(x_2, y_2) \approx I_{20} \sum_m \mu_n b_{m+n}(p) b_m^*(p) T'_\mathrm{s}(x_\mathrm{s} - (m+n)p_\mathrm{s}d_1, y_1) {T'}_\mathrm{s}^*(x_\mathrm{s} - mp_\mathrm{s}d_1, y_1) \exp\left[2\pi i \frac{nx_2}{d_2}\right] \quad . (17)$$

Equation (17) means that this optical configuration works as a multi-wave interferometer: the deformation of the self-image due to the insertion of a sample includes the effect of interference between the $(m+1)$th and $m$th orders. In other words, we can realize a shearing interferometer with a shearing distance of $p_\mathrm{s}d_1$ by retrieving the 1st order Fourier component of the intensity of the self-image. From geometrical consideration (see Fig. 2), it can be shown that the spatial coherence length on the grating that is necessary for the shearing interferometer is given by $pd_1$. This is the reason why the interferometer does not require high-spatial-coherence X-rays. Note that, if the shearing distance is larger than the size of the sample, the interferometer works as a Mach-Zehnder interferometer (an array of Mach-Zehnder interferometers), which provides a phase image (see Fig. 6 (a)) as X-ray and electron holographies do [57,58]. A fringe scanning [59-61] or Fourier transform method [62] is commonly used to retrieve the 1st order Fourier component $q_1(x_2, y_2)$ of the intensity of the self-image. If we neglect the effect of the free-space propagation, i.e., $T'_\mathrm{s}(x_\mathrm{s}, y_\mathrm{s}) \approx T_\mathrm{s}(x_\mathrm{s}, y_\mathrm{s})$, the phase difference between $\Phi(x_\mathrm{s} - (m+1)p_\mathrm{s}d_1, y_\mathrm{s})$ and$\Phi(x_\mathrm{s} - mp_\mathrm{s}d_1, y_\mathrm{s})$ is obtained from the argument of $q_1$. Note that when a rectangular grating with a duty cycle of 0.5 is used and the compression ratio of the self-image is 1, only the three terms $a_{-1}$, $a_0$, $a_1$ contribute to $q_1(x_2, y_2)$, so that the optical configuration works as a three-wave interferometer. In fact, from Eq. (17), the 1st order Fourier component of the intensity of the self-image is proportional to

$$P(x_2, y_2) = \mu_1\big(b_0 b^*_{-1} T_\mathrm{s}(x_\mathrm{s}, y_\mathrm{s}) T^*_\mathrm{s}(x_\mathrm{s} + p_\mathrm{s} d_1, y_\mathrm{s}) + b_1 b^*_0 T_\mathrm{s}(x_\mathrm{s} - p_\mathrm{s} d_1, y_\mathrm{s}) T^*_\mathrm{s}(x_\mathrm{s}, y_\mathrm{s})\big) \exp\left[2\pi i \frac{x_2}{d_2}\right], \quad (18)$$

and for a weakly absorbing sample, the argument of Eq. (18) is proportional to

$$\frac{\Phi(x_\mathrm{s} - p_s d_1, y_\mathrm{s}) - \Phi(x_\mathrm{s} + p_s d_1, y_\mathrm{s})}{2}, \quad (19)$$

which gives a twin image with an opposite sign separated by $2p_s d_1$ [29,30,32], as later shown in Figs. 6(a) and 6(c). Here, we used $(b_0 b^*_{-1})^* = b_1 b^*_0$. Since the configuration gives the twin image, it can be regarded as a quasi-two-wave interferometer, but at points where $\mathit{\Delta} P(x_2, y_2)$ defined by

$$\mathit{\Delta} P(x_2, y_2) \equiv \arg[b_0 b^*_{-1} T_\mathrm{s}(x_\mathrm{s}, y_\mathrm{s}) T^*_\mathrm{s}(x_\mathrm{s} - p_\mathrm{s} d_1, y_\mathrm{s})] - \arg[b_1 b^*_0 T_\mathrm{s}(x_\mathrm{s} + p_\mathrm{s} d_1, y_\mathrm{s}) T^*_\mathrm{s}(x_\mathrm{s}, y_\mathrm{s})], \quad (20)$$

is close to π, the photon number that contributes to form the twin image becomes very small to make the image have a low signal-to-noise ratio. In addition, when $\mathit{\Delta} P(x_2, y_2)$ exceeds an odd-integer multiple of π, π-wrapping, i.e., π-phase jump, occurs [32] (see Fig. 7 (a)). This kind of wrapping is different from that caused by the fact that the range of the value of $\arg[b_0 b^*_{-1} T_\mathrm{s}(x_\mathrm{s}, y_\mathrm{s}) T^*_\mathrm{s}(x_\mathrm{s} + p_\mathrm{s} d_1, y_\mathrm{s}) + b_1 b^*_0 T_\mathrm{s}(x_\mathrm{s} - p_\mathrm{s} d_1, y_\mathrm{s}) T^*_\mathrm{s}(x_\mathrm{s}, y_\mathrm{s})]$ is limited from −π to π; unwrapping algorithms for the latter do not work well for the former because we can experimentally obtain π-wrapped images after they are blurred by the finite size of the X-ray source and/or point spread function of the X-ray image detector.

It is often assumed that $\Phi(x_\mathrm{s}, y_\mathrm{s})$ is a slowly varying function of $x_\mathrm{s}$. In this case,

$\Phi(x_\mathrm{s}, y_\mathrm{s})$ can be expanded by a Taylor series and approximated up to the first order:

$$\Phi(x_\mathrm{s}, y_\mathrm{s} - mp_\mathrm{s}d_1) \approx \Phi(x_\mathrm{s}, y_\mathrm{s}) - mp_\mathrm{s}d_1 \frac{\partial\Phi(x_\mathrm{s}, y_\mathrm{s})}{\partial x_\mathrm{s}}. \quad (21)$$

Thus, by taking the argument of the 1st order Fourier component of the intensity of the self-image, $\arg[q_1]$, we can obtain a differential phase image $\frac{\partial\Phi(x_\mathrm{s}, y_\mathrm{s})}{\partial x_\mathrm{s}}$. Note that there is a tradeoff between the magnification of the sample and the sensitivity to $\frac{\partial\Phi(x_\mathrm{s}, y_\mathrm{s})}{\partial x_\mathrm{s}}$: increasing magnification of the sample makes the slope of the wavefront gentle and, as a result, reduces the sensitivity to $\frac{\partial\Phi(x_\mathrm{s}, y_\mathrm{s})}{\partial x_\mathrm{s}}$. In other words, the effective Talbot order $p_\mathrm{s}$ becomes smaller when the sample is located closer to the X-ray source to increase the magnification of the sample.

There are several setups that have so far been proposed for obtaining the differential phase image. Figure 3 shows four typical setups of the X-ray grating interferometry for this purpose. In the setup shown in Fig. 3(a) [24,38], the self-image generated downstream of a grating (G1) is resolved by a high-spatial-resolution X-ray image detector, and $\arg[q_1]$ was obtained by the Fourier transform method [62], where the spatial resolutions of the obtained images are limited by the pitch of the self-image. Because the setup of Fig. 3(a) requires a high-spatial resolution X-ray image detector, which generally has a small field-of-view, it is suitable only in the case where a small field-of-view is sufficient. The interferometer shown in Fig. 3(b) is called a Talbot interferometer [19,63,64], where an absorption grating (G2) is overlaid on a self-image to form an image with moiré fringes (a moiré image). Generating moiré fringes makes it possible to detect the deformation of the self-image without using a high-resolution X-ray image detector and to realize a large field of view. The setups of Figs. 3(c) [35] and 3(d) [23] enable the use of using a low-brilliance X-ray source. As shown in Section 2, a spatial coherent length that is comparable or larger than the pitch of the grating used is required for the Talbot effect to occur. Because of the weak interaction of hard X-rays with materials, the grating has to have a high aspect-ratio, which makes it difficult to reduce the pitch of the grating to less than 1 μm. Thus, from the van Cittert-Zernike theorem, a micro-focus X-ray source or a very large distance from a large-size X-ray source is necessary to meet the requirement of the spatial coherence length. The setups shown in Figs. 3(c) and 3(d) meet the requirement with even a low-brilliance normal-size X-ray source: the source grating (G0) located close to the X-ray source works as an array of individually coherent but mutually incoherent X-ray sources. In this case, another condition is necessary for the self-images that is generated by the mutually incoherent X-ray sources to constructively be added:

$$\frac{1}{d_0} = \frac{\alpha}{d_1} - \frac{1}{d_2}, \quad (22)$$

where $\alpha$ is the compression ratio of the self-image. The use of a normal-size X-ray source drastically reduces the time that is required for obtaining a moiré image because the X-ray flux that is generated by an X-ray source is generally proportional to the size of the source.

It should be noted that, in addition to the merit that continuous-spectrum spherical-wave X-rays are available, the X-ray grating interferometry has multi-modality: it can provide three independent images called transmittance, differential-phase, and visibility-contrast images

[25,31,36,37,41-47], which can be given by $|q_0|$, $\arg[q_1]$, and $\frac{2|q_1|}{|q_0|}$, respectively. The first image corresponds to the conventional absorption-contrast image, while the contrast of the third image has several origins including mainly ultra-small-angle X-ray scattering from the sample, which enables structure analysis at each pixel.

## 4. X-ray imaging microscopy using self-imaging phenomenon

In Section 2, we saw that the Talbot effect can occur even when a grating is illuminated by continuous-spectrum spherical-wave X-rays and that it enables to realize X-ray phase-contrast imaging. Since a spherical wave can magnify an image, we can construct an X-ray phase-contrast microscope by using the Talbot effect.

The simplest type of X-ray phase-contrast microscopy using the Talbot effect is the projection types that have been shown in Fig. 3. In these cases, their spatial resolutions are determined not only by magnification but also by the total size of the X-ray source and the spatial resolution of the X-ray image detector. To attain a spatial resolution of, e.g., 1 μm using the projection type X-ray phase-contrast microscopy, it is necessary to use an X-ray source with a size less than 1 μm and/or an X-ray image detector with a spatial resolution less than 1 μm, both of which reduce the photon number available for X-ray imaging. In addition, free-space propagation of X-rays from the sample to the X-ray image detector blurs the image of the sample projected on the detector because of refraction caused by the sample, although this blurring causes an edge-enhancement effect, which is positively used for the so-called propagation-based imaging technique.

The setup of the X-ray imaging microscope shown in Fig. 4(a), consisting of an X-ray lens and a grating, can solve the problem of the defocusing. For simplicity, we assume here that the X-ray lens (objective lens) is ideal, i.e., the amplitude spread function (ASF) is given by a delta function. In fact, from detailed analytical calculations, it was shown that the electric field created on the image plane (the $(x'_2, y'_2)$-plane) can be expressed by

$$E_2(x'_2, y'_2) \approx E'_{20} \sum_n b_n(p') T_{\mathrm{s}}(x'_{\mathrm{s}} - np'd'_1, -y'_{\mathrm{s}}) \exp\left[2\pi i \frac{nx'_2}{d'_2}\right], \quad (23)$$

which is the same as that in the case of the X-ray projection microscope shown in Fig. 3(a) except that there is no defocusing effect. Here, $E'_{20}$ corresponds to the electric field on the image plane without the sample and the grating, expressed by

$$E'_{20} = -\frac{\exp\left[\frac{2\pi i(a+b)}{\lambda}\right]\exp\left[\frac{\pi i({x'_2}^2+{y'_2}^2)}{\lambda R'_2}\right]}{M}, \quad (24)$$

where $a$, $b$, and $R'_2$ are geometrically defined distances from the object plane to the X-ray lens, from the X-ray lens to the image plane, and from the focal spot of the X-ray source to the image plane, respectively, $M$ is the magnification of the sample, which is given by $\frac{b}{a}$, and the $(x'_{\mathrm{s}}, y'_{\mathrm{s}})$-plane is defined on the object plane, defined by $(x'_{\mathrm{s}}, y'_{\mathrm{s}}) \equiv -\frac{1}{M}(x'_2, y'_2)$. Equation (23) includes both the cases where the grating is located upstream and downstream of the X-ray lens if we define the Talbot order $p'$ and the pitch $d'_2$ of the Fresnel image on the image plane as follows:

$$p' \equiv \begin{cases} -\frac{\lambda z_{\mathrm{eff,s1}}}{{d'_1}^2} & (R_{\mathrm{s}} \leq R_1 < R_{\mathrm{lens}}) \\ \frac{\lambda z'_{\mathrm{eff,12}}}{{d_1}^2} & (-f' < R'_1 \leq R'_2, R'_1 \neq 0) \end{cases} \quad , (25)$$

$$d'_2 \equiv \begin{cases} Md_{\mathrm{s}} & (R_{\mathrm{s}} \leq R_1 < R_{\mathrm{lens}}) \\ d_1 \frac{R'_2}{R'_1} & (-f' < R'_1 \leq R'_2, R'_1 \neq 0) \end{cases} \quad , (26)$$

where $R_{\mathrm{lens}}$ is the distance of the X-ray lens from the X-ray source, $f'$ is the distance of the focal spot of the X-ray source from the lens, satisfying $\frac{1}{f} = \frac{1}{R_{\mathrm{lens}}} + \frac{1}{f'}$, where $f$ is the focal length of the X-ray lens, $R'_1$ is the distance of the grating from the focal spot when the grating is located downstream of the X-ray lens, $z_{\mathrm{eff,s1}}$ and $z'_{\mathrm{eff,12}}$ are the effective distance defined by

$$z_{\mathrm{eff,s1}} \equiv \left(\frac{1}{R_{\mathrm{s}}} + \frac{1}{R_1 - R_{\mathrm{s}}}\right)^{-1} \quad , (28)$$

$$z'_{\mathrm{eff,12}} \equiv \left(\frac{1}{R'_1} + \frac{1}{R'_2 - R'_1}\right)^{-1} \quad , (29)$$

and $d_{\mathrm{s}} \equiv d_1 \frac{R_{\mathrm{s}}}{R_1}$. Equation (23) can be interpreted as follows: when the grating is located between the object plane and the X-ray lens, a Fresnel image corresponding to a negative Talbot order is virtually generated on the object plane, which forms a magnified Fresnel image on the image plane with the magnification of $M$, whereas when the grating is located between the X-ray lens and image plane, the focal spot of the X-ray source works as a virtual X-ray source and a Fresnel image with a positive and negative Talbot order is generated on the image plane by the spherical-wave X-rays from the virtual focal spot. Here, it was assumed that the X-ray lens is ideal, i.e., the amplitude spread function (ASF) is given by a delta function, but for a real lens, the electric field on the image plane is convoluted with the ASF [30].

The spatial coherence length on the object plane that is necessary for the Talbot effect to occur is roughly given by $d'_2/M$ [30]. This is equivalent to the condition that the spatial coherence length of the spherical-wave X-rays from the virtual focal spot on the image plane is comparable or larger than $d'_2$.

Because Eq. (23) is the same as that in the case of the X-ray projection microscope except for without the defocusing effect, we can realize X-ray phase contrast microscopy using the self-imaging phenomenon. Similar to the setups of the X-ray phase-contrast imaging shown in Fig. 3, several setups are possible for the X-ray phase-contrast microscopy. Figures 4(b), 4(c), and 4(d) demonstrate typical possible setups of an X-ray phase-contrast microscope consisting of two or three gratings. In the setup shown in Fig. 4(b), an absorption grating overlays the self-image on the image plane to form a moiré image, from the deformation of which a differential-phase image is obtained. The setup shown in Fig. 4(d) is similar but uses a source grating, the image of which works as an array of individually coherent but mutually incoherent virtual X-ray sources. This setup enables the use of a low-brilliance X-ray source. The spatial resolution of both the setups of Figs. 4(b) and 4(d) is limited by the pitch of the absorption grating on the image plane. In addition, increasing magnification $M$ makes the slope of the wavefront gentle and, as a result, reduces the sensitivity to $\frac{\partial\Phi(x_s,y_s)}{\partial x_s}$, similarly to the setup of Figs. 3(b) and (d).

A solution that solves the problem of the low spatial resolution and the reduced sensitivity is highly magnifying and resolving the self-image, which can be realized by the setups shown in

Figs. 4(a) and 4(c). In these setups, their spatial resolution is not limited by the pitch of the grating and even the total size of the low-brilliance X-ray source but is mainly determined by the numerical aperture of the X-ray lens. In addition, instead of a differential-phase image, we can obtain a twin image with an opposite sign separated by $2p'd'_1$, each of which is a phase image if the sample is smaller than the separation distance $2p'd'_1$ (later shown in Figs. 6(a) and 6(c)). Thus, they enable quantitative X-ray phase-contrast imaging without the loss of sensitivity. A phase image can also be retrieved from a twin image for a sample larger than $2p'd'_1$, as later shown in Fig. 6(d).

## 5. Experimental examples

It was experimentally shown that the setups shown in Figs. 4(a), 4(b), and 4(c) work as X-ray phase-contrast microscopes. The first experiment of X-ray phase-contrast microscopy using the self-imaging phenomenon was performed by Takeda *et al*. in the setup of Fig. 4(b). The setup was constructed at BL20XU, SPring-8, Japan, where a high-spatial coherence monochromatic X-ray beam from an undulator is available at an experimental station located 245 m downstream from the source. They used 12.4 keV monochromatic X-rays from a double-crystal monochromator, a Fresnel zone plate with an outermost zone width of 100 nm and a focal length of 320 mm as an X-ray lens, 8 μm-pitch $\pi/2$-phase and absorption gratings, and an X-ray image monochromator detector with an effective pixel size of 4.34 μm consisting of a phosphor screen, a relay lens, and a cooled charge-coupled device (CCD) camera. Figure 5(a) is a moiré image detected on the image plane. A differential phase image of polystyrene (PS) spheres and a Ta test chart with a magnification of 18.4 were successfully obtained by a fringe scanning method with a higher sensitivity than that based on X-ray absorption contrast without the grating (Figs. 5(b) and 5(c)). It was shown that the spatial resolution of these images is limited by the pitch of the grating. X-ray phase tomography was also performed for a piece of PS/PMMA blend, and its phase-separation structure consisting of PS-rich and PMMA-rich regions was successfully observed (Fig. 5 (d)).

Higher spatial resolution and higher sensitivity X-ray phase-contrast imaging was also successfully realized by Yashiro *et al.* in the setup of Fig. 4(a) [29,30,32]. This experiment was also performed at BL20XU, SPring-8. Monochromatic X-rays with an energy of 9 keV, a Fresnel zone plate with an outermost zone width of 86.6 nm and a focal length of 261 mm, and the X-ray image detector with an effective pixel size of 4.34 μm were used and a 4.3 μm-pitch $\pi/2$-phase grating was located 67.8 mm downstream from the back focal plane of the lens.

Figures 6(a) and 6(c) show twin images of PS spheres and a 1-μm-thick Siemens star chart with a magnification of 23.7 obtained by a fringe scanning method. It was shown that the twin image of Fig. 6(a) gives quantitative phase images and has much higher sensitivity than that based on X-ray absorption contrast without the grating (Fig. 6(b)). In addition, the spatial resolution achieved by the setup was not limited by the pitch of the grating but by the numerical aperture of the lens and the spatial resolution of the detector. In Fig. 6 (a), the standard deviation in the region without the sample was $2\pi \times 0.003$ rad. A phase image of the Siemens star chart was also successfully retrieved (Fig. 6 (d)) by an adaptive deconvolution algorithm using the visibility-contrast image, which is simultaneously obtained in the fringe scanning method and proportional to the signal-to-noise ratio of the twin image.

The setup proposed by Yashiro *et al*. enables quantitative X-ray phase-contrast imaging even for a sample with a large phase shift, which is essential for X-ray phase tomography but difficult to perform using conventional Zernike-phase-contrast X-ray imaging. Figure 7 demonstrates an example of quantitative X-ray phase-contrast imaging and tomography for a PS sphere with a diameter of 55 μm obtained by Yashiro *et al.* In this case, not only the 2π-wrapping due to the fact that the range of the value of argument function is limited from $-\pi$ to $\pi$ but also the π-wrapping mentioned in Section 3 can be seen between the twin image in Fig. 7(a). They extracted the boundaries of the π-wrapped regions by using the fact that this π-phase jump occurs when $|q_1|$ is close to zero, which performed unwrapping successfully. From such quantitative X-ray phase-contrast images after the π-unwrapping (an example is shown in Fig. 7(c)), a phase tomogram of the PS sphere was successfully obtained (Fig. 7(e)).

The setup shown in Fig. 4(c) was also attained by Kuwabara *et al.* using a low-brilliance normal-focus laboratory X-ray source [34]. They used a rotating anode-type X-ray source with a size of 0.2 (horizontal) and 0.3 mm (vertical). A pyrolytic graphite (PG) mosaic crystal was used as a monochromator to use Cu K$\alpha_1$ characteristic X-rays. Taking the so-called Bragg-Brentano geometry, the PG crystal worked as a condenser of X-rays to illuminate the sample. Figure 8 shows a twin image (8(b)) and a phase image (8(d)) of an 8.8-μm-thick polyimide film with a magnification of 5.4. Although the spatial resolution in this case was limited by the spatial resolution of the X-ray image detector because of the limited magnification in a limited space, quantitative X-ray phase-contrast microscopy using the self-imaging phenomenon and a low-brilliance X-ray source was successfully performed. Recently, Takano *et al*. achieved a spatial resolution of 50 nm with the same setup except that they used high-performance Fresnel zone plate and capillary condenser optics [50].

## 6. Prospects and conclusions

As is seen in Section 2, the self-imaging phenomenon occurs even in the case of continuous-spectrum spherical-wave X-rays. This means that the development of an achromatic X-ray lens for high-spatial resolution with a small coma aberration would make it possible to realize high-spatial and temporal resolution X-ray phase contrast microscopy using a wideband width of a pink undulator beam or a white synchrotron X-ray beam from a bending magnet. Wolter mirrors [65,66] are candidates for an X-ray lens without chromatic and coma aberrations, but it is difficult to fabricate an Wolter mirror for imaging with a spatial resolution less than 100nm [67,68]. Recently, Matsuyama *et al*. successfully developed advanced Kirkpatrick-Baez (AKB) mirrors [69], which are a system for X-ray imaging microscopy consisting of two elliptical mirrors and two hyperbolic mirrors oriented perpendicular to each other, and attained a spatial resolution of 50 nm without chromatic aberration [70,71]. The use of such an achromatic X-ray imaging system will expand the possibility of the X-ray phase-contrast imaging microscopy introduced in this review.

Future development of an energy-resolved X-ray image detector will also open a new window: in addition to X-ray phase-contrast imaging microscopy, X-ray fluorescent imaging microscopy may be simultaneously achieved in the same setup. Thus, the X-ray phase-contrast microscopy using the self-imaging phenomenon is a promising tool for various fields including materials sciences, biology, medicine, and industrial applications.

Note that the Talbot-Lau interferometer works not only for X-rays but also neutrons [72-81] and matter waves [17,82-86]. The setup of the microscope for a low-brilliance X-ray source introduced in this review will enable high-spatial resolution phase-contrast imaging even with neutrons and matter waves from incoherent sources if high-performance lenses are developed for them.

In conclusion, X-ray phase-contrast microscopy using the self-imaging phenomenon provides a high sensitivity, brought by the use of the X-ray phase shift, and a high spatial resolution which is not limited by the pitch of the grating and the total size of the X-ray source but by the numerical aperture of the X-ray lens, and makes it possible to even use a low-brilliance X-ray source. This approach has several advantages over the conventionally proposed X-ray imaging microscopy and can provide a powerful way of quantitative visualization in various fields of materials and life sciences.

## Acknowledgements

Part of the research introduced in this review was supported by Grants-in-Aid for Scientific Research (B) (Grant No. 19360027) from the Ministry of Education, Culture, Sports, Science and Technology and Japan Science and Technology Agency (JST) CREST Grant Number JPMJCR1765.

## References

[1] Sakdinawat A and Attwood D (2010), Nanoscale X-ray imaging, *Nat. Photonics* **4**, 840-848.

[2] Fitzgerald R (2000), Phase-sensitive x-ray imaging, *Phys. Today* **53**, 23–26.

[3] Momose A (2005), Recent advances in x-ray phase imaging, *Jpn. J. Appl. Phys.* **44**, 6355–6367.

[4] Nugent K A (2010), Coherent methods in the X-ray sciences, *Adv. Phys.* **59**, 1–99.

[5] Zernike F (1935), The phase contrast process in microscopic examinations, *Phys. Z.* **36** 848 [in German].

[6] Born M and Wolf E (1999), *Principles of Optics*. (Cambridge University Press, Cambridge.)

[7] Kagoshima Y, Ibuki T, Yokoyama Y, Tsusaka Y, Matsui J, Takai K, and Aino M (2001), 10 keV X-ray phase-contrast microscopy for observing transparent specimens, *Jpn. J. Appl. Phys*. **40**, L1190-1192.

[8] Izzo J R, Joshi A S, Grew K N, Chiu W K S, Tkachuk A, Wang S H, and Yun W B (2008), Nondestructive reconstruction and analysis of SOFC anodes using x-ray computed tomography at sub-50 nm resolution, *J. Electrochem. Soc.* **155**, B504-508.

[9] Stampanoni M, Mokso R, Marone F, Vila-Comamala J, Gorelick S, Trtik P, Jefimovs K, and David C (2010), Phase-contrast tomography at the nanoscale using hard x rays, *Phys. Rev. B* **81**, 140105(R).

[10] Holzner C, Feser M, Vogt S, Hornberger B, Baines S B, and Jacobsen C (2010), Zernike phase contrast in scanning microscopy with X-rays, *Nat. Phys.* **6**, 883-887.

[11] Cowley J M and Moodie A F (1957), Fourier images: Ⅰ—The point source, *Proc. Phys. Soc. B* **70**, 486-496.

[12] Talbot H F (1836), Facts relating to optical science, *Philos. Mag.* **9**, 401–407.

[13] Patorski K (1989), The Self-Imaging Phenomenon and its Applications, *Prog. Opt.* **27**, 1-108.

[14] Cowley W D (1995), *Diffraction Physics.* (Elsevier Science B. V., Amsterdam.)

[15] Mansuripur M (2002), Talbot effect, In: Classical Optics and its Applications, Chap. 18 (Cambridge University Press, Cambridge).

[16] Wen J, Zhang Y, and Xiao M (2013), The Talbot effect: recent advances in classical optics, nonlinear optics, and quantum optics, *Adv. Opt. Photonics* **5**, 83-130.

[17] Clauser J F and Reinsch M W (1992), New theoretical and experimental results in Fresnel optics with applications to matter-wave and X-ray interferometry, *Appl. Phys.* B **54**, 380-395.

[18] David C, Nöhammer B, and Solak H H (2002), Differential x-ray phase contrast imaging using a shearing interferometer, *Appl. Phys. Lett.* **81**, 3287-3289.

[19] Momose A, Kawamoto S, Koyama I, Hamaishi Y, Takai K, and Suzuki Y (2003), Demonstration of X-Ray Talbot interferometry, *Jpn. J. Appl. Phys.* **42**, L866-L868.

[20] Weitkamp T, Nöhammer B, Diaz A, David C, and Ziegler E (2005), X-ray wavefront analysis and optics characterization with a grating interferometer, *Appl. Phys. Lett.* **86**, 054101.

[21] Weitkamp T, Diaz A, David C, Pfeiffer F, Stampanoni M, Cloetens P, and Ziegler E (2005), X-ray phase imaging with a grating interferometer, *Opt. Express* **13**, 6296-6304.

[22] Momose A, Yashiro W, Takeda Y, Suzuki Y, and Hattori T (2006), Phase tomography by X-ray Talbot interferometry for biological imaging, *Jpn. J. Appl. Phys.* **45**, 5254-5262.

[23] Pfeiffer F, Weitkamp T, Bunk O, and David C (2006), Phase retrieval and differential

phase-contrast imaging with low-brilliance X-ray sources, *Nat. Phys.* **2**, 258-261.

[24] Takeda Y, Yashiro W, Suzuki Y, Aoki S, Hattori T, and Momose A (2007), X-ray phase imaging with single phase grating, *Jpn. J. Appl. Phys*. **46**, L89-L91.

[25] Pfeiffer F, Weitkamp T, Bunk O, and David C (2008), Hard-X-ray dark-field imaging using a grating interferometer, *Nat. Mater.* **7**, 134-137.

[26] Yashiro W, Takeda Y, and Momose A (2008), Efficiency of Capturing a Phase Image using Cone-beam X-ray Talbot Interferometry, *J. Opt. Soc. Am. A* **25**, 2025-2039.

[27] Takeda Y, Yashiro W, Hattori T, Takeuchi A, Suzuki Y, and Momose A (2008), Differential Phase X-ray Imaging Microscopy with X-ray Talbot Interferometer, *Appl. Phys. Express* **1**, 117002.

[28] Momose A, Yashiro W, Maikusa H, and Takeda Y (2009), High-speed X-ray phase imaging and X-ray phase tomography with Talbot interferometer and white synchrotron radiation, *Opt. Express* **17**, 12540-12545.

[29] Yashiro W, Takeda Y, Takeuchi A, Suzuki Y, and Momose A (2009), Hard-X-Ray Phase-Difference Microscopy Using a Fresnel Zone Plate and a Transmission Grating, *Phys. Rev. Lett.* **103**, 180801.

[30] Yashiro W, Harasse S, Takeuchi A, Suzuki Y, and Momose A (2010), Hard-x-ray phase-imaging microscopy using the self-imaging phenomenon of a transmission grating, *Phys. Rev. A* **82**, 043822.

[31] Yashiro W, Terui Y, Kawabara K, and Momose A (2010), On the origin of visibility contrast in x-ray Talbot interferometry, *Opt. Express* **18**, 16890-16901.

[32] Yashiro W, Harasse S, Kuwabara H, Mizutani H, Takeuchi A, Suzuki Y, and Momose A (2011), X-ray Phase Imaging and Tomography Using a Fresnel Zone Plate and a Transmission Grating, *AIP conference Proceedings* **1365**, 317-320.

[33] Momose A, Yashiro W, Harasse S, and Kuwabara H (2011), Four-dimensional X-ray phase tomography with Talbot interferometry and white synchrotron radiation: dynamic observation of a living worm, *Opt. Express* **19**, 8423-8432.

[34] Kuwabara H, Yashiro W, Harasse S, Mizutani H, and Momose A (2011), Hard-X-ray Phase-Difference Microscopy with a Low-Brilliance Laboratory X-ray Source, *Appl. Phys. Express* **4**, 062502.

[35] Momose A, Kuwabara H, and Yashiro W (2011), X-ray Phase Imaging Using Lau Effect, *Appl. Phys. Express* **4**, 066603.

[36] Modregger P, Scattarella F, Pinzer B R, David C, Bellotti R, and Stampanoni M (2012), Imaging the Ultrasmall-Angle X-Ray Scattering Distribution with Grating Interferometry, *Phys. Rev. Lett.* **108**, 048101.

[37] Potdevin G, Malecki A, Biernath T, Bech M, Jensen T H, Feidenhans'l R, Zanette I, Weitkamp T, Kenntner J, Mohr J, Roschger P, Kerschnitzki M, Wagermaier W, Klaushofer K, Fratzl P, and Pfeiffer F (2012), X-ray vector radiography for bone micro-architecture

diagnostics, *Phys. Med. Biol.* **57**, 3451-3461.

[38] Matsuyama S, Yokoyama H, Fukui R, Kohmura Y, Tamasaku K, Yabashi M, Yashiro W, Momose A, Ishikawa T, and Yamauchi K (2012), Wavefront measurement for a hard-X-ray nanobeam using single-grating interferometry, *Opt. Express* **20**, 24977-24986.

[39] Wen H, Gomella A A, Patel A, Lynch S K, Morgan N Y, Anderson S A, Bennett E E, Xiao X, Liu C, and Douglas E. Wolfe D E (2013), Subnanoradian X-ray phase-contrast imaging using a far-field interferometer of nanometric phase gratings, *Nat. Commun.* 4:2659.

[40] Wang H C, Berujon S, Pape I, Sawhney K (2013), X-ray microscopy using two phase contrast imaging techniques: two dimensional grating interferometry and speckle tracking, *J. Phys. Conf. Ser.* **463**, UNSP 012042.

[41] Schaff F, Malecki A, Potdevin G, Eggl E, Noël P B, Baum T, Garcia E G, Bauer J S, and Pfeiffer F (2014), Correlation of X-Ray Vector Radiography to Bone Micro-Architecture, *Sci. Rep.* **4**, 3695.

[42] Malecki A, Potdevin G, Biernath T, Eggl E, Willer K, Lasser T, Maisenbacher J, Gibmeier J, Wanner A, and Pfeiffer F (2014), X-ray tensor tomography, EPL **105**, 38002.

[43] Yashiro W and Momose A (2014), Grazing-incidence ultra-small-angle X-ray scattering imaging with X-ray transmission gratings: A feasibility studey, *Jpn. J. Appl. Phys.* **53**, 05FH04.

[44] Modregger P, Kagias M, Peter S, Abis M, Guzenko V A, David C, and Stampanoni M

(2014), Multiple Scattering Tomography, *Phys. Rev. Lett.* **113**, 020801.

[45] Modregger P, Rutishauser S, Meiser J, David C, and Stampanoni M (2014), Two-dimensional ultra-small angle X-ray scattering with grating interferometry, *Appl. Phys. Lett.* **105**, 024102.

[46] Bayer F L, Hu S, Maier A, Weber T, Anton G, Michel T, and Riess C P (2014), Reconstruction of scalar and vectorial components in X-ray dark-field tomography, *PNAS* **111**, 12699-12704.

[47] Yashiro W and Momose A (2015), Effects of unresolvable edges in grating-based X-ray differential phase imaging, *Opt. Express* **23**, 9233-9251.

[48] Miao H, Panna A, Gomella A A, Bennett E E, Znati S, Chen L, and Wen H (2016), A universal moiré effect and application in X-ray phase-contrast imaging, *Nat. Phys.* **12**, 830-836.

[49] Yashiro W, Noda D, and Kajiwara K (2017), Sub-10-ms X-ray tomography using a grating interferometer, *Appl. Phys. Express* **10**, 052501.

[50] Takano H, Wu Y, and Momose A (2017), Development of full-field x-ray phase-tomographic microscope based on laboratory x-ray source, *Proc. SPIE* **10391**, 1039110.

[51] Yashiro W, Ueda R, Kajiwara K, Noda D, and Kudo H (2017), Millisecond-order X-ray phase tomography with compressed sensing, *Jpn. J. Appl. Phys*. **56**, 112503.

[52] Yashiro W, Noda D, and Kajiwara K (2018), Effect of insufficient temporal coherence on

visibility contrast in X-ray grating interferometry, *Opt. Express* **26**, 1012-1027.

[53] Lord Rayleigh F R S (1881), XXV. On copying diffraction-gratings, and on some phenomena connected therewith, *Philos. Mag*. **11**, 196-205

[54] Guigay J P (1971), Fresnel Diffraction by one-dimensional periodic objects, with application to structure determination of phase objects, *Opt. Acta* **18**, 677.

[55] Arrizón V and López-Olazagasti E (1995), Binary phase grating for array generation at 1/16 of Talbot length, *J. Opt. Soc. Am. A* **12**, 801-804.

[56] Winthrop J T and Worthington C R, Theory of Fresnel Images. I. Plane Periodic Objects in Monochromatic Light, *J. Opt. Soc. Am* **55**, 373-381.

[57] Eisebitt S, Lüning J, Schlotter W. F., Lörgen M, Hellwig O, Eberhardt W, and Stöhr J (2004), Lensless imaging of magnetic nanostructures by X-ray spectro-holography, *Nature* **432**, 885.

[58] Tonomura A (1987), Applications of electron holography, *Rev. Mod. Phys.* **59**, 639-669.

[59] Bruning J H, Herriott D R, Gallagher J E, Rosenfeld D P, White A D, and Brangaccio D J (1974), Digital Wavefront Measuring Interferometer for Testing Optical Surfaces and Lenses, *Appl. Opt.* **13**, 2693-2703.

[60] H. Schreiber and J. H. Bruning (2007), Phase Shifting Interferometry. In: *Optical Shop Testing*, ed. Malacara D, Chap. 14, (John Wiley & Sons, Inc., Hoboken, New Jersey).

[61] Hack E and Burke J (2011), Invited Review Article: Measurement uncertainty of linear

phase-stepping algorithms, *Rev. Sci. Instrum.* **82**, 061101.

[62] Takeda M, Ina H, and Kobayashi S (1982), Fourier-Transform Method of Fringe-Pattern Analysis for Computer-based Topography and interferometry, *J. Opt. Soc. Am.* **72**, 156-160.

[63] Yokozeki S, and Suzuki T (1971), Shearing Interferometer using grating as beam splitter, *Appl. Opt.* **10**, 1575.

[64] Lohman A W and Silva D E, An interferometer based on the Talbot effect (1971), *Opt. Commun.* **2**, 413-415.

[65] Wolter H (1952), Glancing Incidence Mirror Systems as Imaging Optics for X-rays, *Ann. Phys.* **10**, 94-114 [in German].

[66] Wolter H (1952), A Generalized Schwarzschild Mirror System For Use at Glancing Incidence for X-ray Imaging, *Ann. Phys.* **10**, 286-295 [in German].

[67] Takeuchi A, Suzuki Y, Uesugi K, and Aoki S (2001), At wavelength focusing properties evaluation of the Wolter type grazing incidence mirror, *Nucl. Instrum. Methods. A* **467-468**, 302-304.

[68] Hoshino M, Ishino T, Namiki T, Yamada N, Watanabe N, and Aoki S (2007), Application of a charge-coupled device photon-counting technique to threedimensional element analysis of a plant seed (alfalfa) using a full-field x-ray fluorescence imaging microscope, *Rev. Sci. Instrum.* **78**, 073706.

[69] Kodama R, Ikeda N, Kato Y, Katori Y, Iwai T, Takeshi K (1996), *Opt. Lett.* **21**, 1321-1323.

[70] Matsuyama S, Kidani N, Mimura H, Sano Y, Kohmura Y, Tamasaku K, Yabashi M, Ishikawa T, and Yamauchi K (2012), Hard-X-ray imaging optics based on four aspherical mirrors with 50 nm resolution, *Opt. Express* **20**, 10310-10319.

[71] Matsuyama S, Yasuda S, Yamada J, Okada H, Kohmura Y, Yabashi M, Ishikawa T, and Yamauchi K (2017), 50-nm-resolution full-field X-ray microscope without chromatic aberration using total-reflection imaging mirrors, *Sci. Rep.* **7**, 46358.

[72] Grünzweig C, David C, Bunk O, Dierolf M, Frei G, Kühne G, Kohlbrecher J, Schäfer R, Lejcek P, Ronnow H M R, and Pfeiffer F (2008), Neutron decoherence imaging for visualizing bulk magnetic domain structures, *Phys. Rev. Lett.* **101**, 025504.

[73] Grünzweig C, David C, Bunk O, Dierolf M, Frei G, Kuhne G, Schafer R, Pofahl S, Ronnow H M R, and Pfeiffer F (2008), Bulk magnetic domain structures visualized by neutron dark-field imaging, *Appl. Phys. Lett.* **93**, 112504.

[74] Strobl M, Grünzweig C, Hilger A, Manke I, Kardjilov N, David C, and Pfeiffer F (2008), Neutron Dark-Field Tomography, *Phys. Rev. Lett.* **101**, 123902.

[75] Lee S W, Hussey D S, Jacobson D L, Sim C M, and Arif M (2009), Development of the grating phase neutron interferometer at a monochromatic beam line, *Nuc. Inst. Meth. A* **605**, 16-20.

[76] Strobl M, Hilger A, Kardjilov N, Ebrahimi O, Keil S, and Manke I (2009), Differential

phase contrast and dark field neutron imaging, *Nuc. Inst. Meth. A* **605**, 9-12.

[77] Manke I, Kardjilov N, Schäfer R, Hilger A, Strobl M, Dawson M, Grünzweig C, Behr G, Hentschel M, David C, Kupsch A, Lange A, and Banhart J (2010), Three-dimensional imaging of magnetic domains, *Nat. Commun.* **1**, 125.

[78] Grünzweig C, Kopecek J, Betz B, Kaestner A, Jefimovs K, Kohlbrecher J, Gasser U, Bunk O, David C, Lehmann E, Donath T, and Pfeiffer F (2013), Quantification of the neutron dark-field imaging signal in grating interferometry, *Phys. Rev. B* **88**, 125104.

[79] Strobl M (2014), General solution for quantitative dark-field contrast imaging with grating interferometers, *Sci. Rep.* **4**, 7243.

[80] Strobl M , Betz B, Harti R P, Hilger A, Kardjilov N, Manke I, Grünzweig C (2016), Wavelength-dispersive dark-field contrast: micrometre structure resolution in neutron imaging with gratings, *J. Appl. Crystallogr.* **49**, 569-573.

[81] Seki Y, Shinohara T, Parker J D, Yashiro W, Momose A, Kato H, Sadeghilaridjani M, Otake Y, and Kiyanagi Y (2017), Development of Multi-colored Neutron Talbot-Lau Interferometer with Absorption Grating Fabricated by Imprinting Method of Metallic Glass, J. Phys. Soc. Jpn. **86**, 044001.

[82] Gerlich S, Hackermuller L, Hornberger K, Stibor A, Ulbricht H, Gring M, Goldfarb F, Savas T, Mueri M, Mayor M, Arndt M (2007), A Kapitza–Dirac–Talbot–Lau interferometer for highly polarizable molecules, *Nat. Phys.* **3**, 711-715.

[83] Cronin A D, Schmiedmayer J, Pritchard D E (2009), Optics and interferometry with atoms and molecules, *Rev. Mod. Phys.* **81**, 1051-1129.

[84] Hornberger K , Gerlich S, Haslinger, P, Nimmrichter S, Arndt M (2012), *Rev. Mod. Phys.* **84**, 157-173.

[85] Juffmann T, Milic A, Mullneritsch M, Asenbaum P, Tsukernik A, Tuxen J, Mayor M, Cheshnovsky O, Arndt M (2012), Real-time single-molecule imaging of quantum interference, *Nat. Nanotechnol.* **7**, 296-299.

[86] Eibenberger S, Gerlich S, Arndt M, Mayor M, Tuxen J (2013), Matter-wave interference of particles selected from a molecular library with masses exceeding 10000 amu, *Phys. Chem. Chem. Phys.* **15**, 14696-14700.

CAPTIONS

Fig. 1: (Color online) Illustration of setup where Talbot effect occurs.

Fig. 2: (Color online) Schematic illustration of geometrical-optics interpretation of Talbot effect for monochromatic X-rays. Electric field at distance $z_{12}$ downstream of grating (G1) is formed from interference of waves passing through points $\mathrm{P}_n$ on G1 ($n = 0, \pm1, \pm2, \cdots$), where $\mathrm{P}_n$ is separated at distance of $\Delta x_n$ from $\mathrm{P}_0$. Here, $\Delta l_n$ is optical path difference between *n*th and 0th order.

Fig. 3: (Color online) Four typical setups for X-ray grating interferometry where one (a), two ((b) and (c)), and three (d) gratings are used. Setups illustrated in (b), (c), and (d) are referred to as Talbot, Lau, and Talbot-Lau types.

Fig. 4: (Color online) Four typical setups for X-ray phase-contrast microscopy using self-imaging phenomenon where one (a), two ((b) and (c)), and three (d) gratings are used.

Fig. 5: (a) Moiré image obtained on image plane in X-ray phase-contrast imaging microscopy shown in Fig. 4 (b). (b) Differential phase image of PS spheres obtained by microscopy (left) and transmittance image of them obtained without two gratings (right). (c) Differential phase

image of Ta test chart with thickness of 500 nm obtained by microscopy (upper) and transmittance image of them obtained without two gratings (lower). (d) Three-dimensional rendering view of portion of piece of polystyrene/poly(methyl methacrylate) (PS/PMMA) polymer blend[27] (Copyright (2008) The Japan Society of Applied Physics).

Fig. 6: Twin images obtained in X-ray phase contrast microscopy shown in Fig. 4 (a) ((a) polystyrene (PS) spheres and (c) 1-μm-thick Ta Siemens star chart). (b) Image of PS spheres based on absorption contrast without grating. (d) Phase image of Siemens star chart retrieved by adaptive deconvolution algorithm[29,30] (©2009-2010 American Physical Society).

Fig. 7: (a) Twin image of polystyrene (PS) sphere with diameter of 55 μm. (b) $\ln(|q_1|)$ map. (c) Phase image of PS sphere. (d) Section profile along line A in (c). (e) Tomogram along line B in (c)[32] (©2011 American Institute of Physics).

Fig. 8: (Color online) (a) Self-image without sample. (b) Twin image of triangle-shaped polyimide film with thickness of 8.8 μm (gray scale: $-\pi$ to $\pi$). (c) Section profile along dashed line in (b) (in unit of rad; filled circles: experimental data, dashed line: calculated curve for ideal (high-resolution) X-ray image detector, solid line: result of convolution of dashed line with LSF of X-ray image detector). (d) Phase image retrieved from (b) (gray scale: 0 to $\pi$)[34]

(Copyright (2011) The Japan Society of Applied Physics).

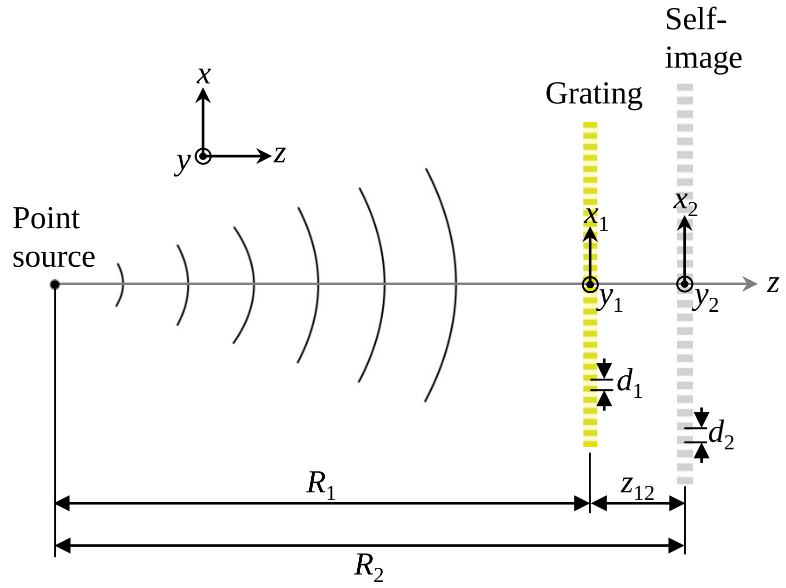

Fig. 1 Wataru Yashiro

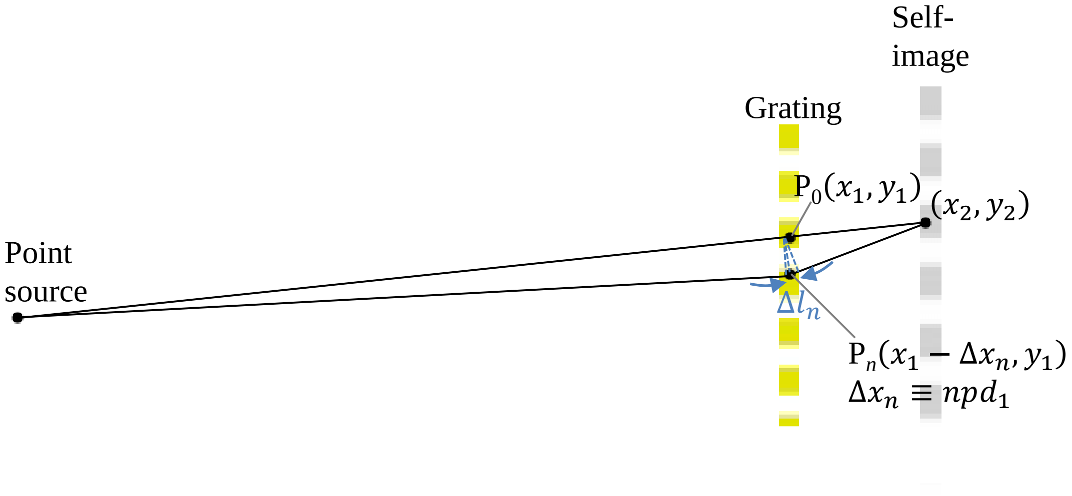

Figure 2 Wataru Yashiro

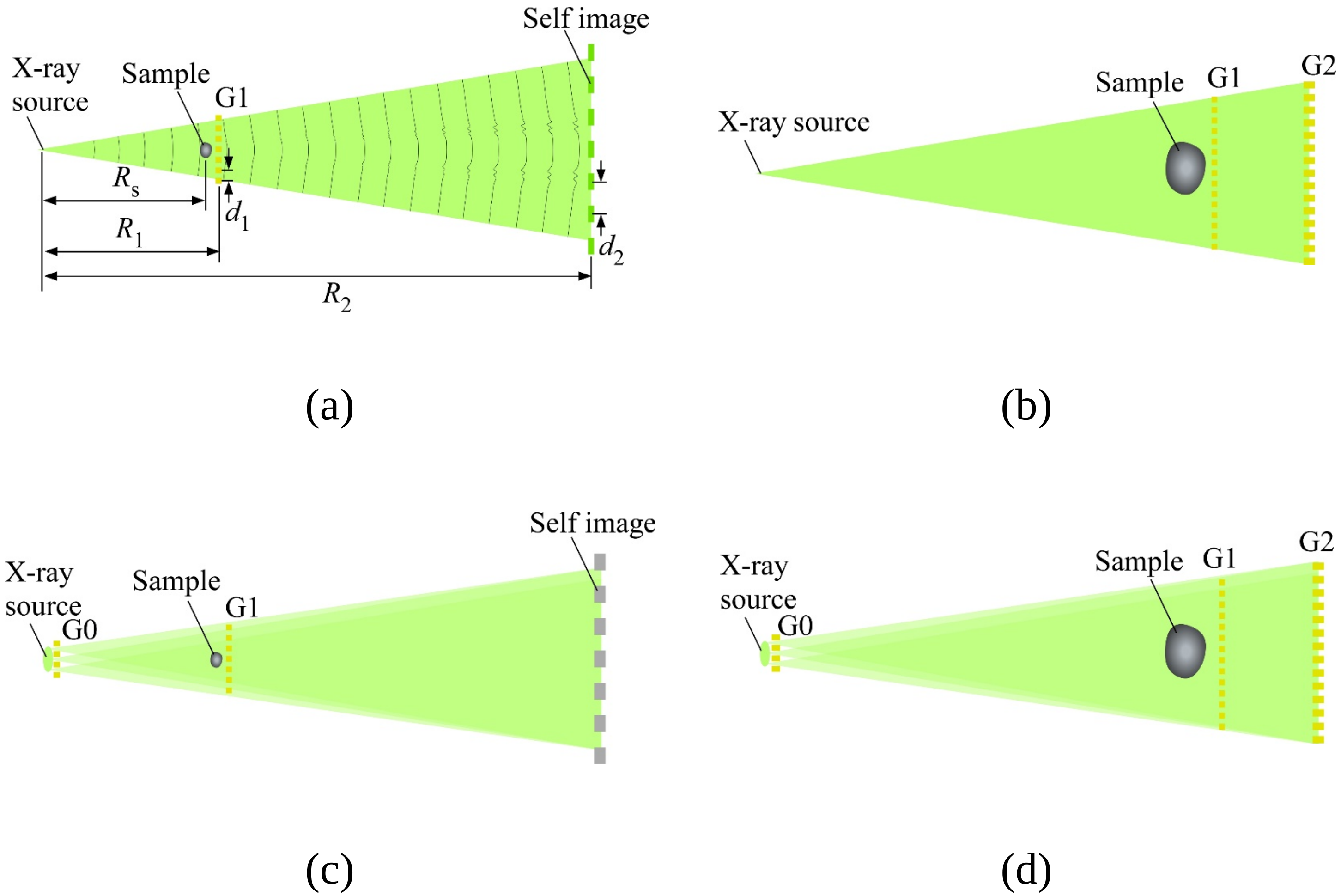

Figure 3 Wataru Yashiro

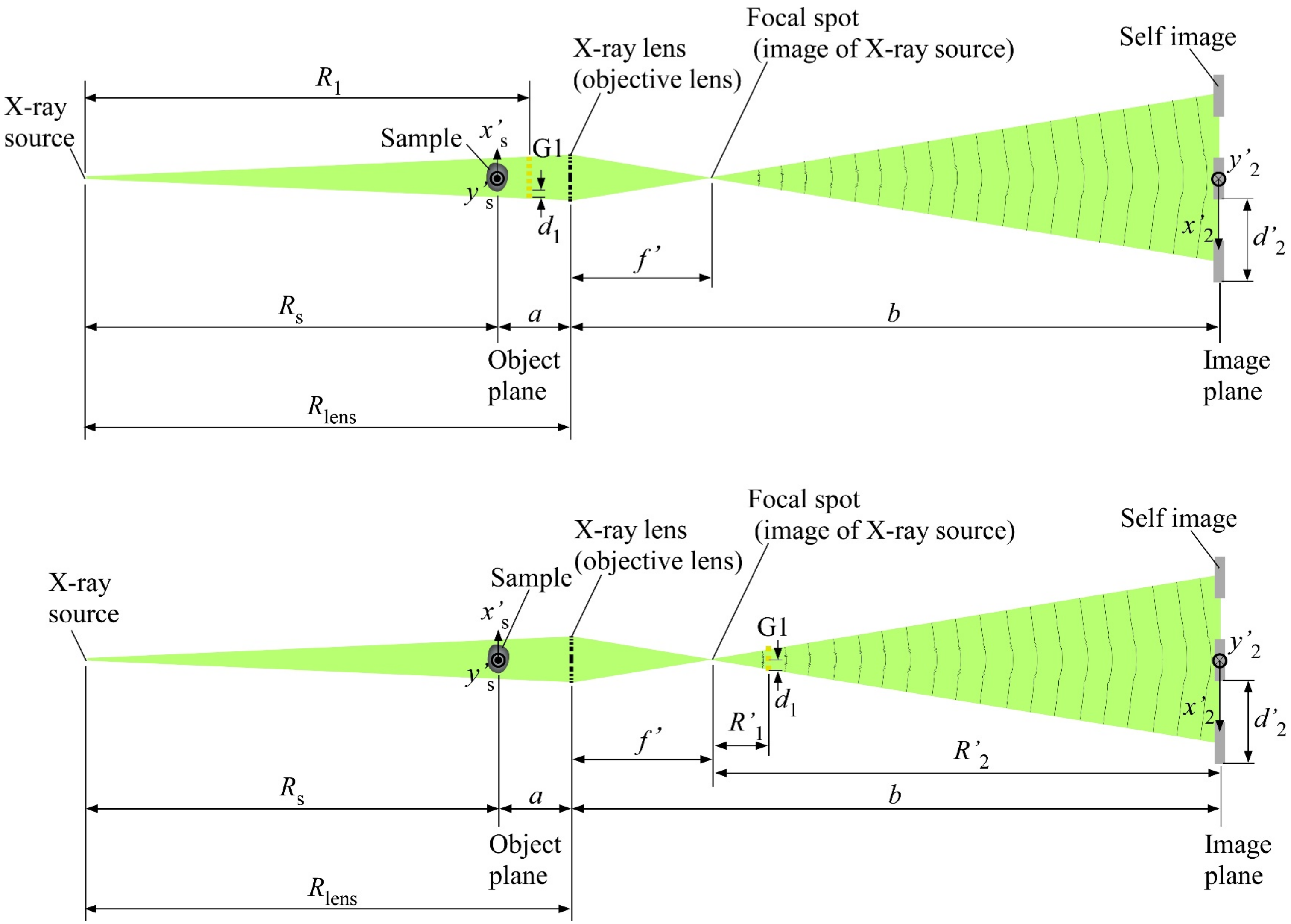

Figure 4(a) Wataru Yashiro

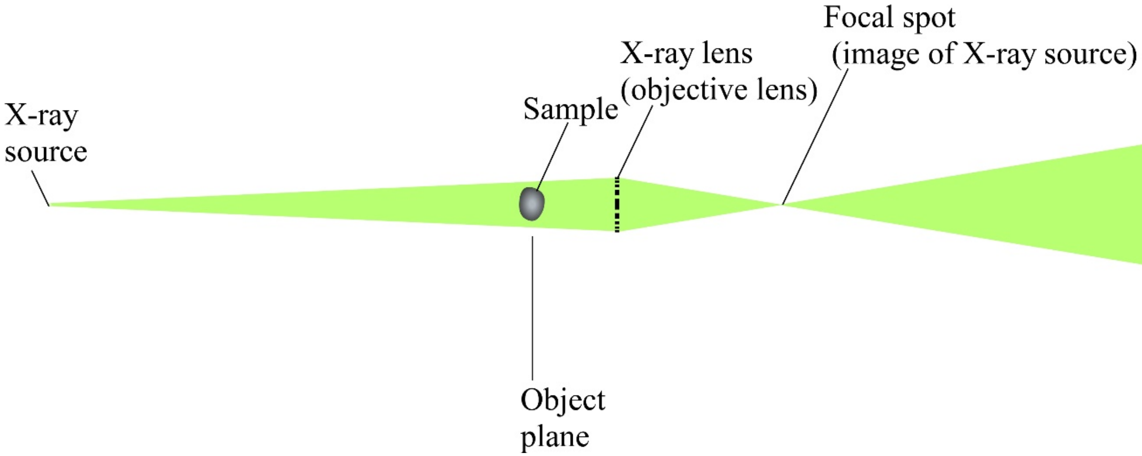

Figure 4(b) Wataru Yashiro

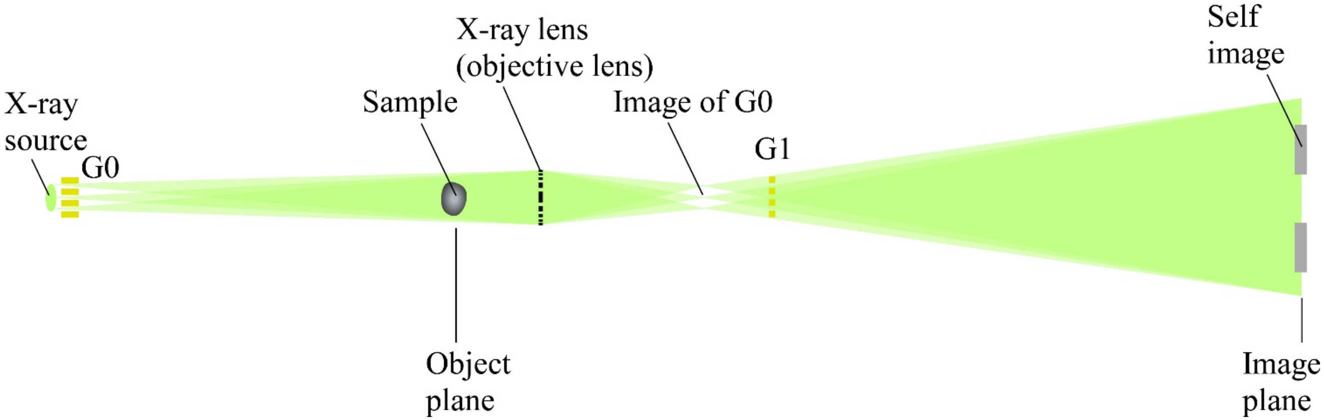

Figure 4(c) Wataru Yashiro

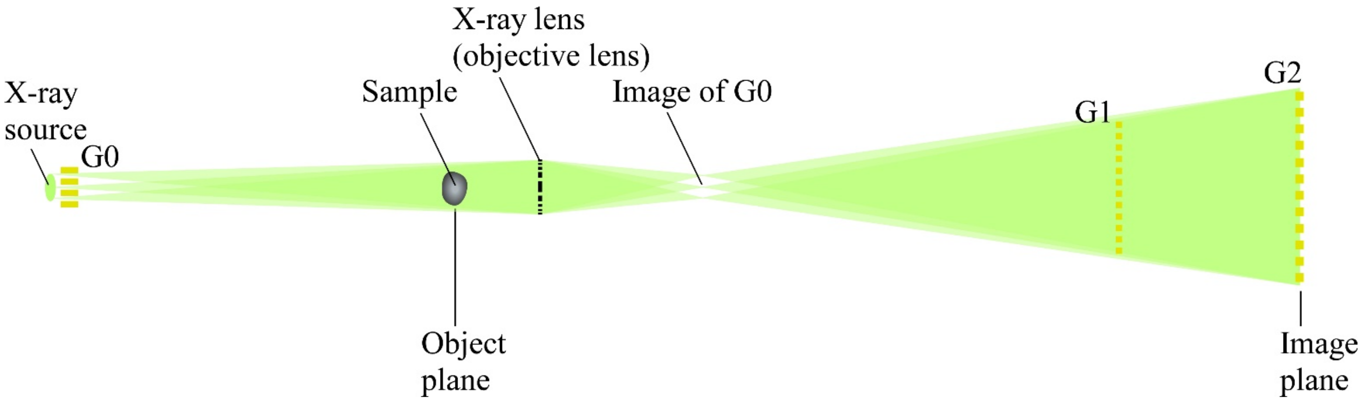

Figure 4(d) Wataru Yashiro

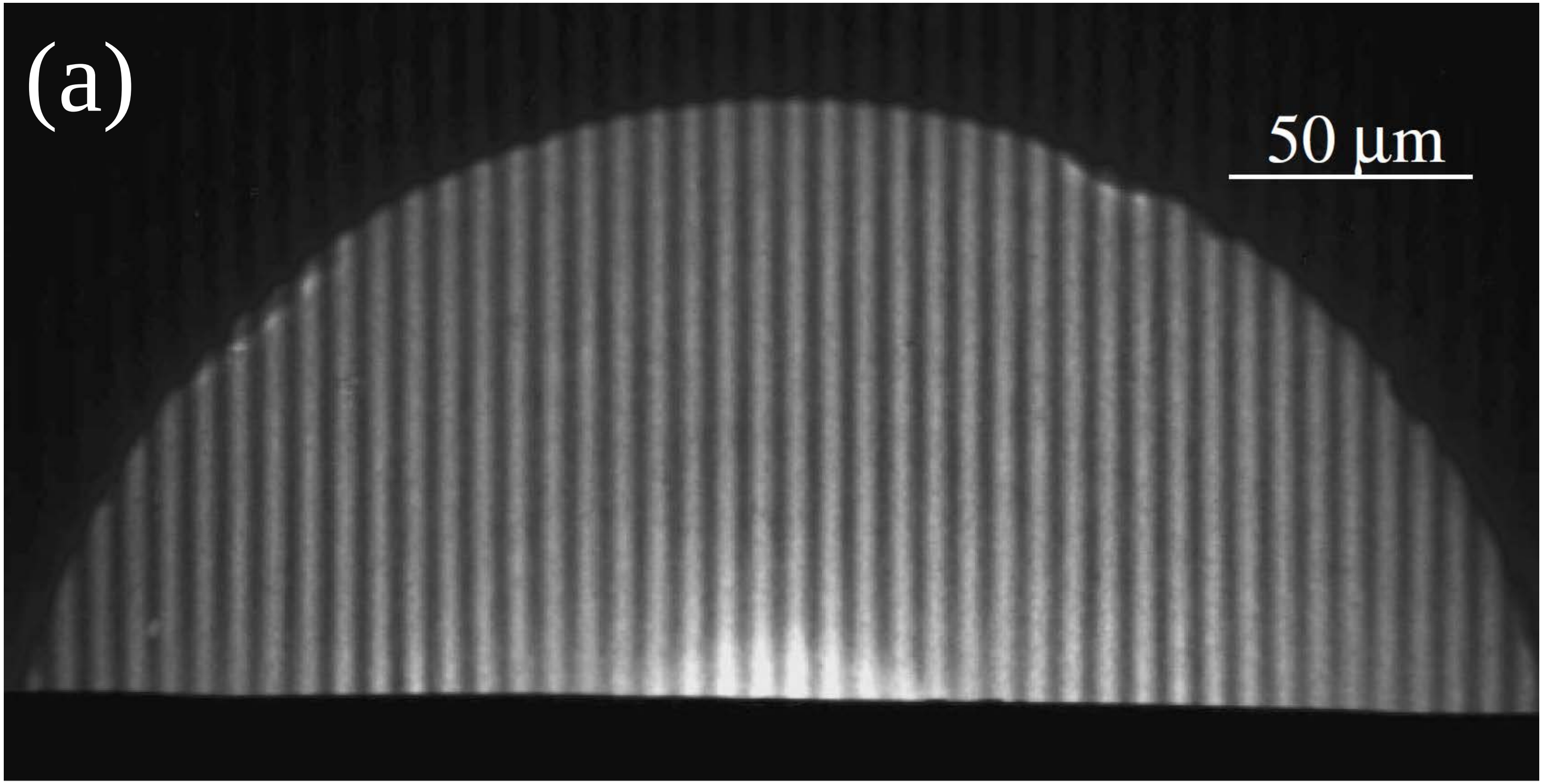

Figure 5 (a) Wataru Yashiro

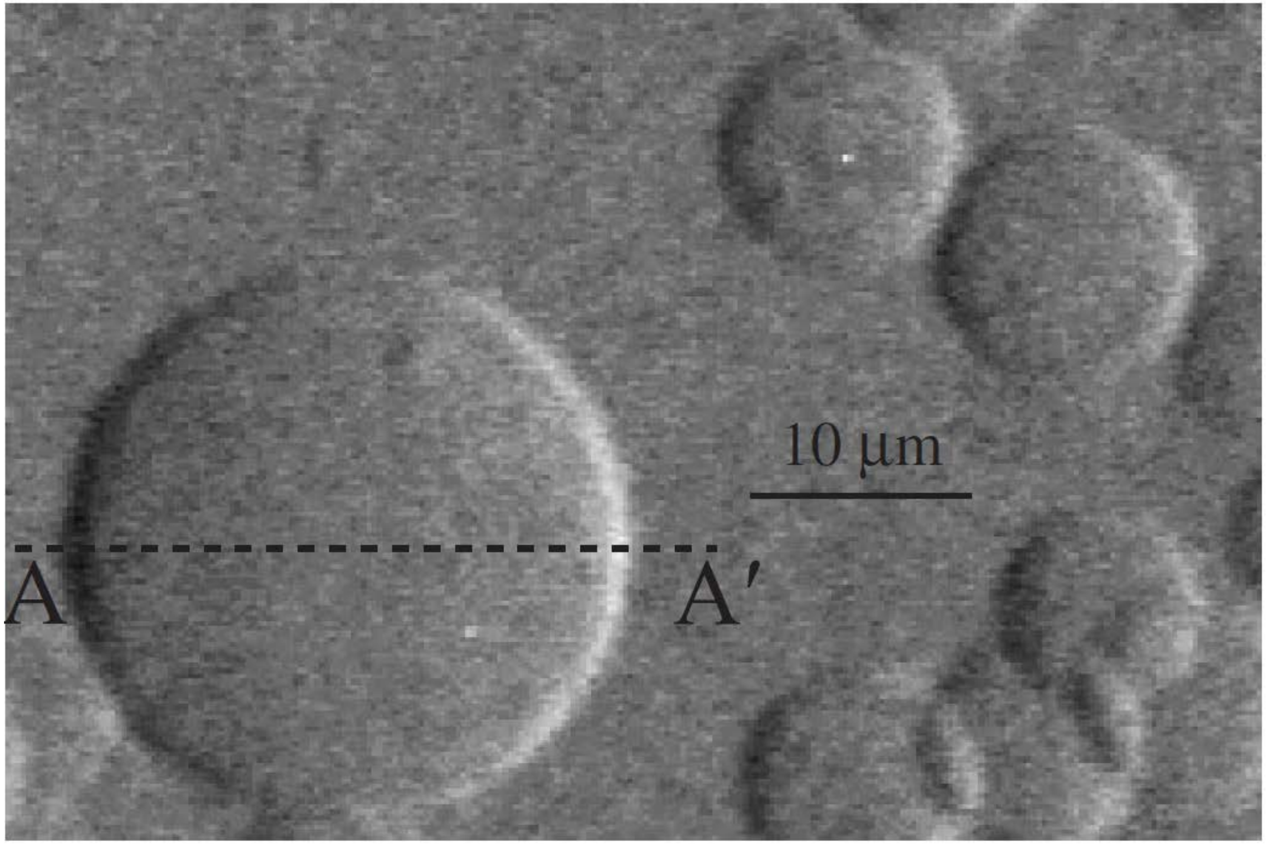

Figure 5 (b) left Wataru Yashiro

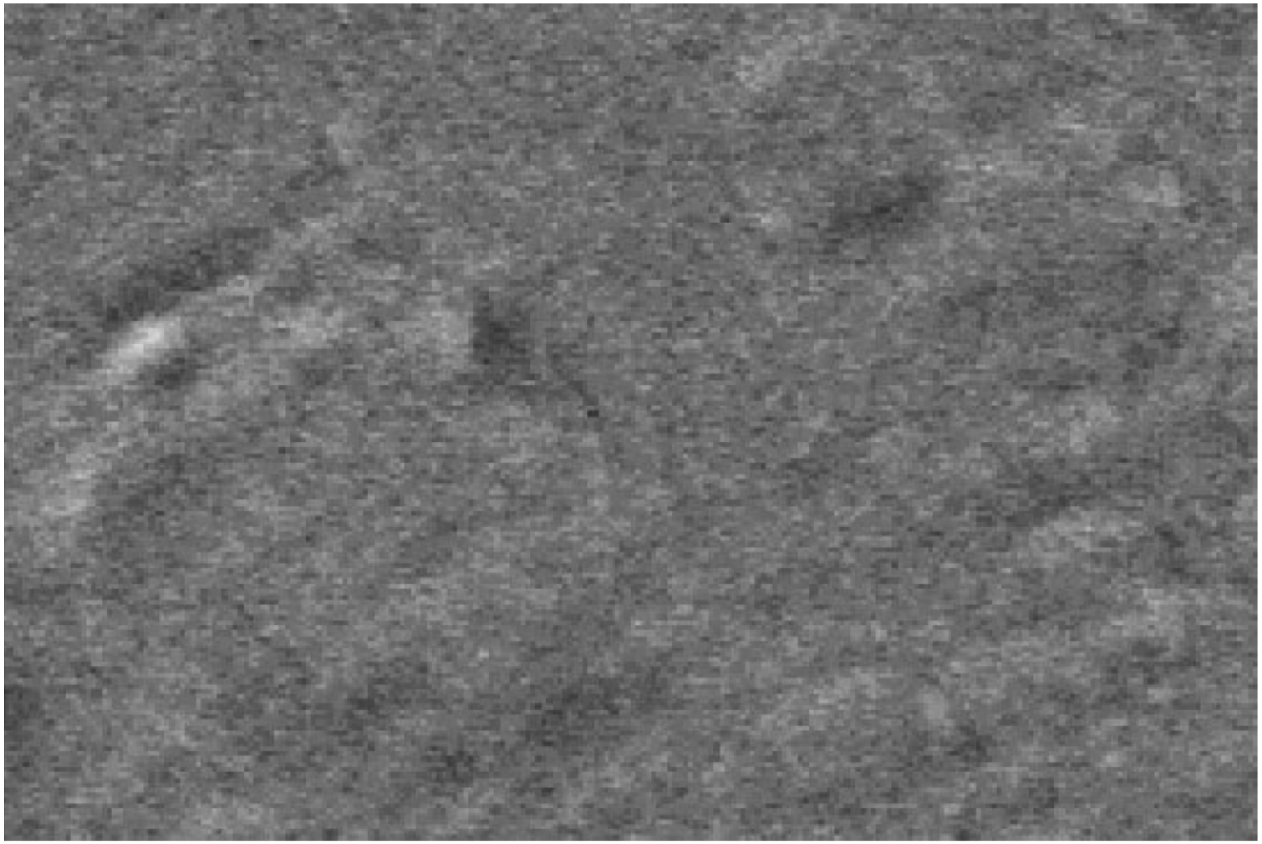

Figure 5 (b) right Wataru Yashiro

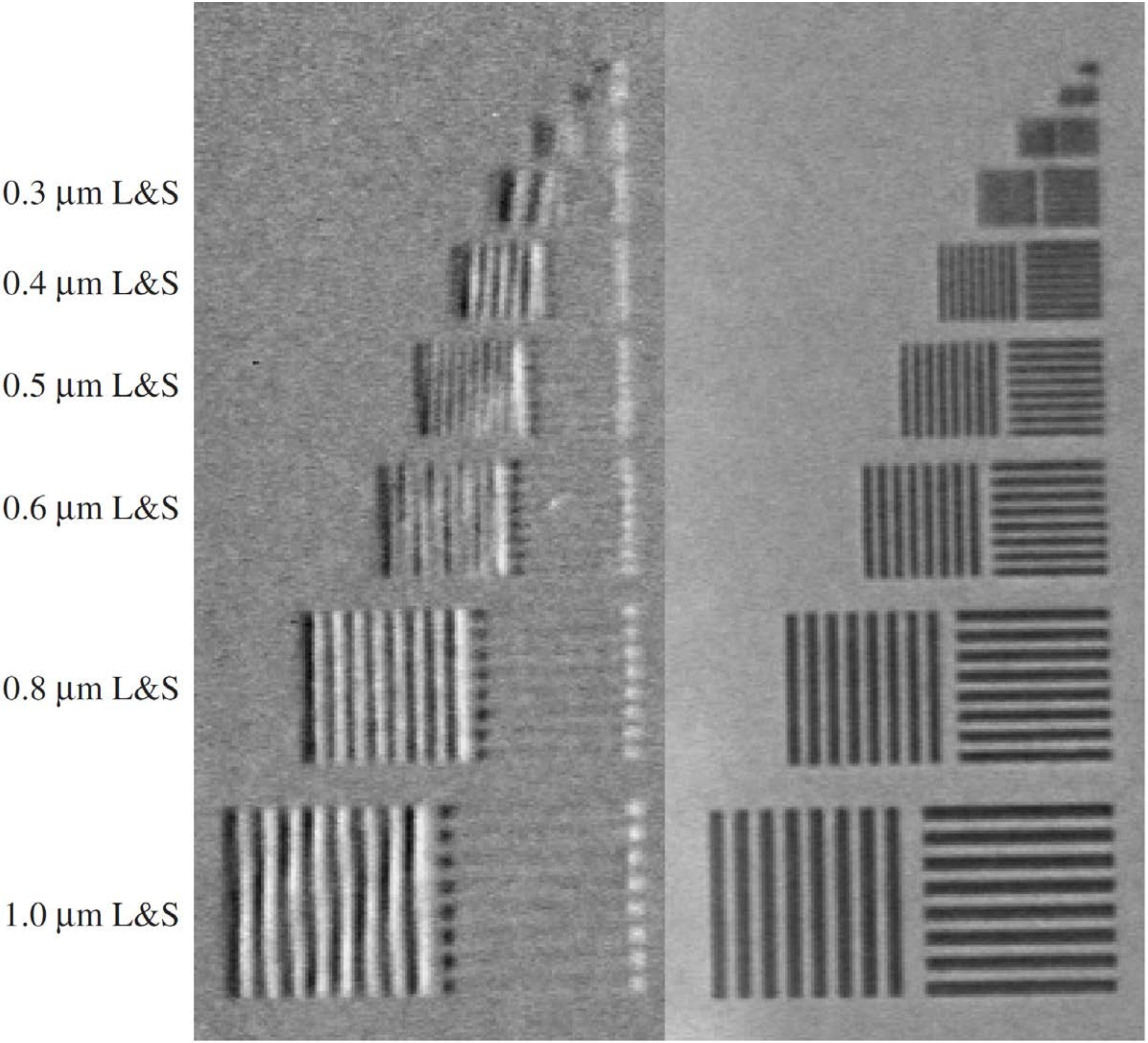

Figure 5 (c)
Wataru Yashiro

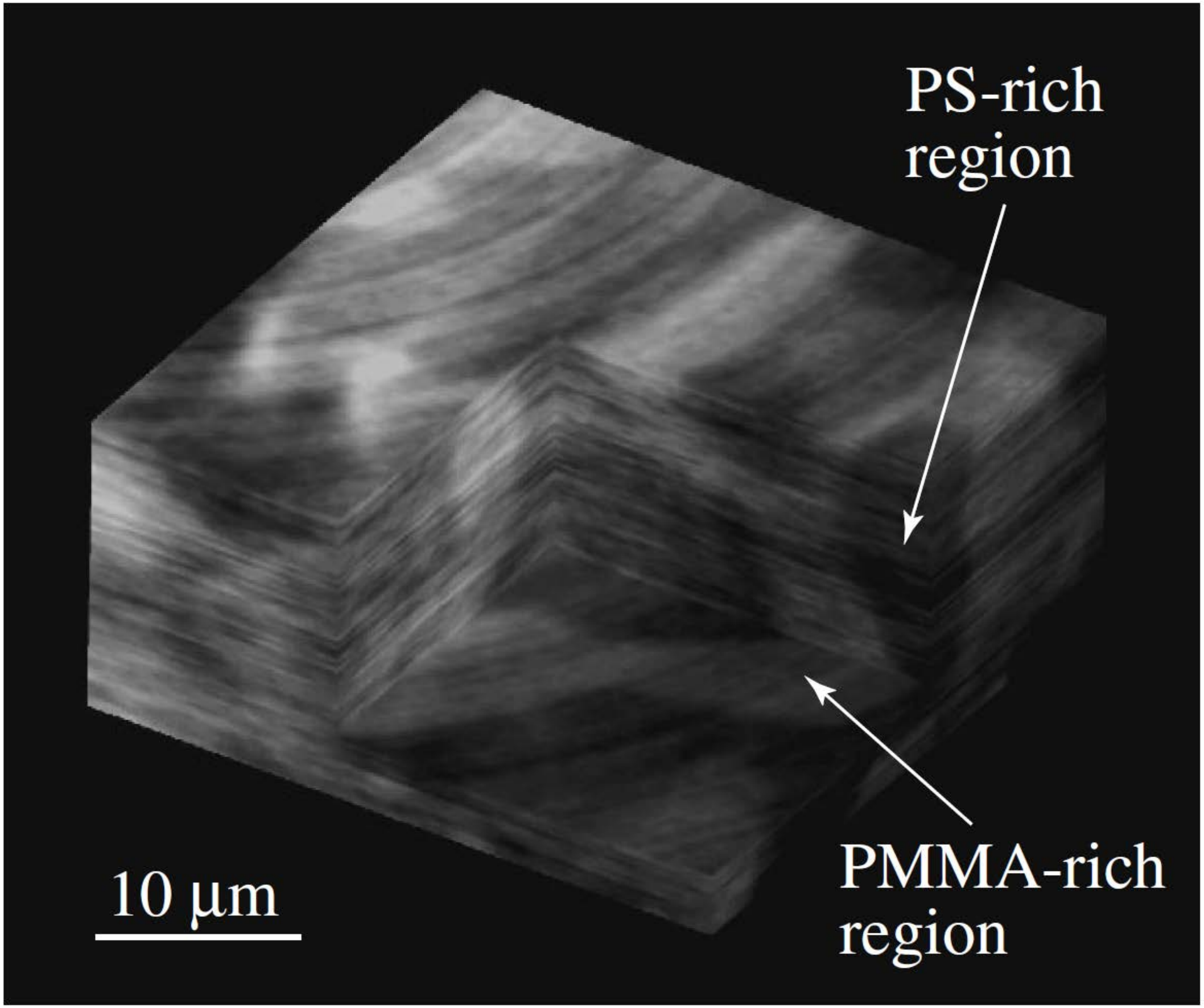

Figure 5 (d) Wataru Yashiro

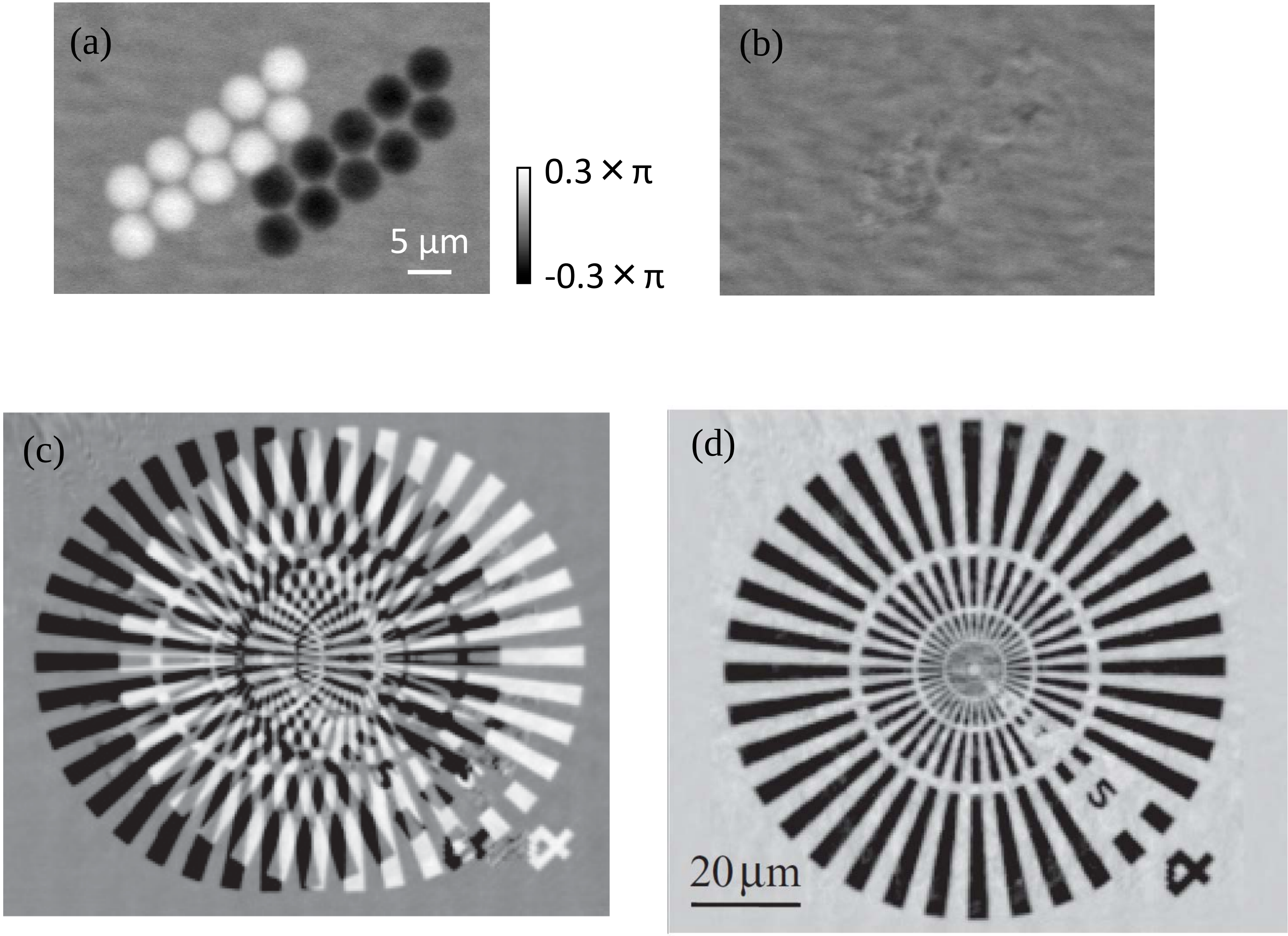

Figure 6 Wataru Yashiro

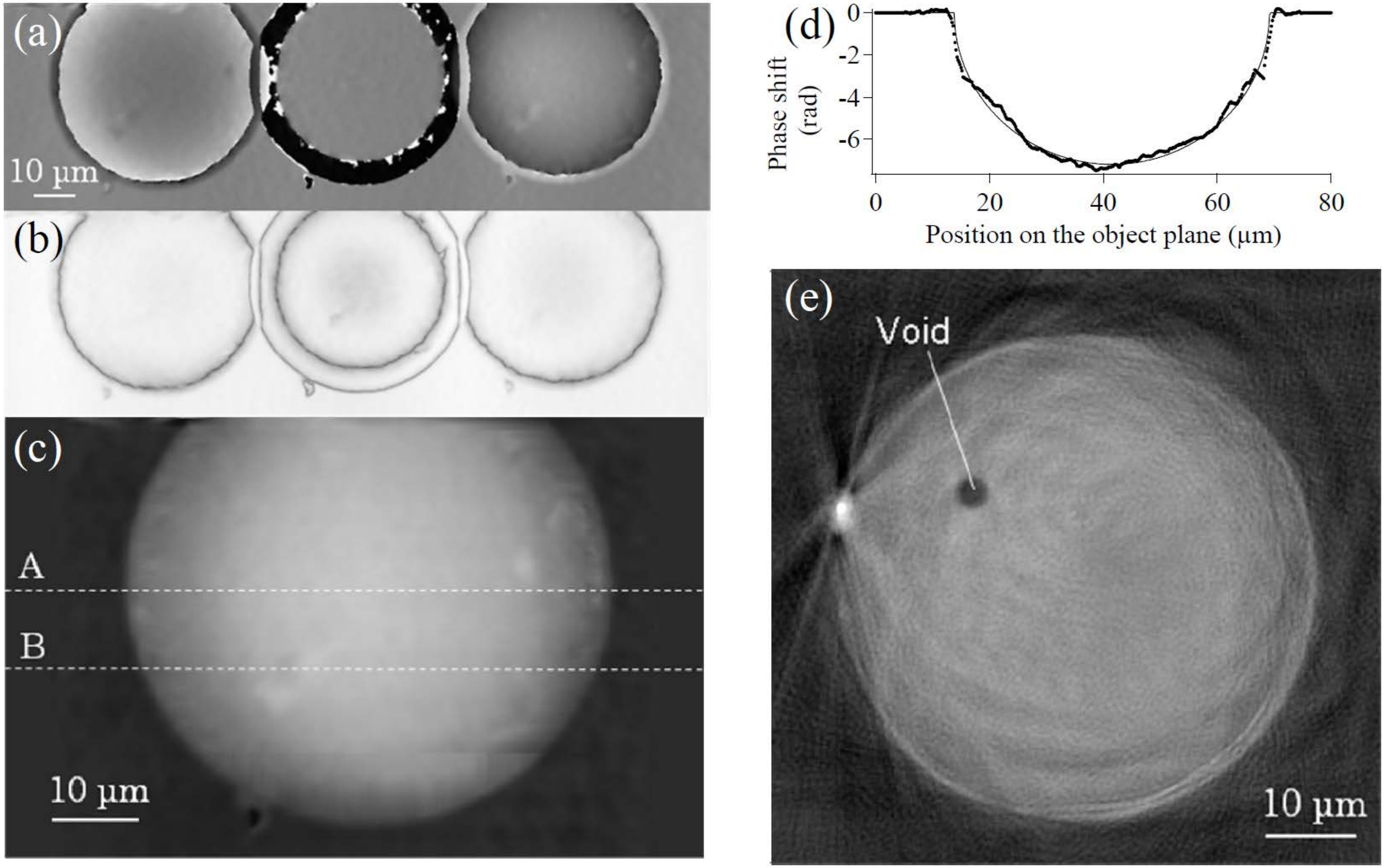

Figure 7 Wataru Yashiro

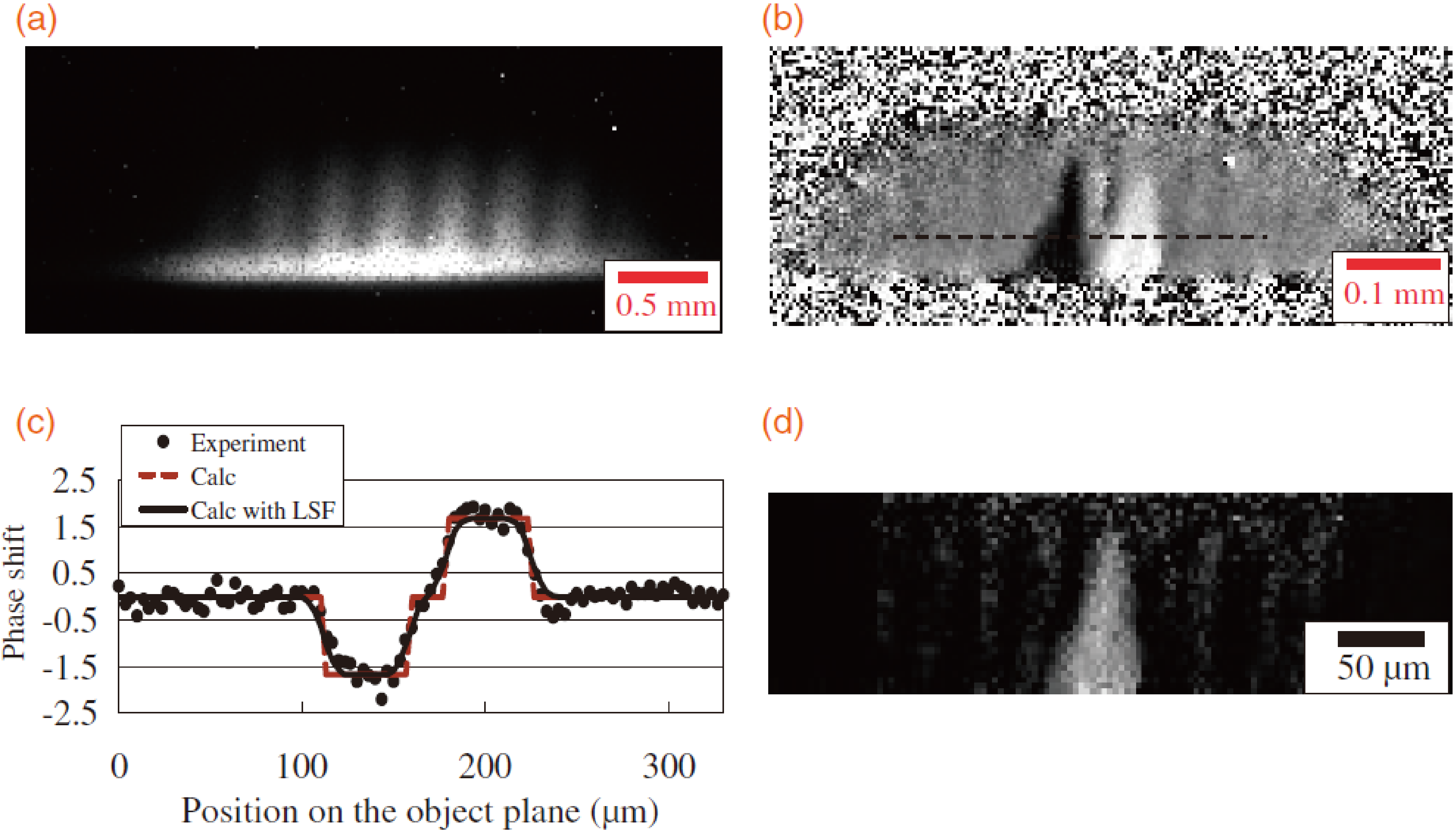

Figure 8 Wataru Yashiro